

Next-Generation Solid-State Quantum Emitters

by

Nachiket Sunil Sherlekar

A thesis
presented to the University of Waterloo
in fulfillment of the
thesis requirement for the degree of
Master of Applied Science
in
Electrical and Computer Engineering

Waterloo, Ontario, Canada, 2019

© Nachiket Sherlekar 2019

I hereby declare that I am the sole author of this thesis. This is a true copy of the thesis, including any required final revisions, as accepted by my examiners.

I understand that my thesis may be made electronically available to the public.

Abstract

This thesis details two types of deterministic solid-state quantum emitters, an optically-driven quantum dot source in a tapered nanowire waveguide, and an electrically-driven source implemented by integrating a single-electron pump into a two-dimensional p-n junction.

A finite-difference time-domain model of the optically-driven nanowire quantum dot source yielded optimized architectural parameters required to obtain a high transmission efficiency and a Gaussian far-field emission profile. An additional model of an electrically-gated nanowire source examined the effect of the surrounding structures on the emission properties of the source.

A successfully working prototype p-n junction device as a precursor to the electrically-driven quantum emitter was implemented by simultaneously inducing positive and negative two-dimensional carrier gases in an undoped semiconductor heterostructure. This device, fabricated in-house, offers a path forward in the development of a new class of bright, deterministic sources of single- and entangled-photons.

Acknowledgements

The highs and lows of experimental research cannot be navigated without a large amount of help from a lot of different people. Having constantly supportive colleagues, friends and family to celebrate my successes and commiserate my setbacks has aided me immensely during the course of my degree.

I would first like to thank all my fellow members of the QPD group, current and former, for their friendship and guidance. Particularly, Mohammed Zeeshan and Arash Ahmadi for your endless patience and willingness to try and answer any and all questions I have; sharing an office with the two of you has been a great experience.

Since the beginning, my advisor Michael Reimer has been constantly supportive and attentive of his students, and has helped foster a wholesome and hard-working lab environment, for which I am deeply thankful. Thank you for your guidance, patience and kindness.

I would like to especially thank my collaborators, François Sfigakis and Brandon Buonacorsi. You have collectively expanded my scientific and technical knowledge by vast amounts, and helped me hone my tenacity and work ethic in a way that is sure to aid me greatly in my future.

Listing the name of every individual who has kept me sane and helped me grow as a person during the past couple of years would take up too much space; what follows is an attempt at abbreviating this list. Shout-out to Manjit Grewal, Jérémy Béjanin, Nina Feng, Rahul Deshpande, Kayla Hardie, Morgan Mastrovich, Anand Lopez, Júlia Amorós Binefa, Annelise Bergeron, Kristine Boone, Doug Braden, Chris Warren, Johan Israelian, Kavish Kaup, Kissan Mistry, Aly Mitha, Thomas Alexander, Jeremy Flannery, Aditya Jain, Cliff Plesha, Ramy Tannous, Thendral Govindraj and Christine and John Dietrich for being amazing friends.

Lastly, I would like to thank my family for their love and support, for instilling in me the desire to always learn new things and improve myself, and for their willingness to grow along with me.

Table of Contents

List of Figures	viii
List of Tables	x
1 Introduction	1
1.1 Historical background	2
1.2 The ideal quantum emitter	4
1.3 Thesis overview	5
2 Bright, deterministic quantum light generation	7
2.1 Optically-driven semiconductor quantum dots	8
2.1.1 The biexciton-exciton cascade	8
2.1.2 Erasure of fine structure splitting	12
2.2 Electrically-driven quantum light sources	14
2.2.1 Two-dimensional carrier systems	14
2.2.2 Single-parameter electron pumps	20
2.3 Collection structures	22
2.3.1 Micropillar cavities	24
2.3.2 Tapered nanowires	25

3	Nanowire quantum dot source model	27
3.1	Parameter sweep to maximize brightness	28
3.2	Gated nanowire quantum dot source	33
4	Design and testing of all-electric quantum emitter	34
4.1	Diode architecture	35
4.1.1	Substrate wafer specifications and mesa	36
4.1.2	Ohmic contacts	37
4.1.3	Top-gate and bond pads	37
4.2	2DEG/2DHG characterization	38
4.2.1	Magnetoresistance	39
4.2.2	Carrier densities and mobilities	41
4.2.3	I-V measurements	43
4.3	Diode behaviour	44
5	Summary & future work	47
5.1	Gated nanowire source optimized for brightness	48
5.2	Integrating an electron pump and a narrow p-n junction	48
	Letter of copyright permission	50
	Bibliography	52
A	Lumerical FDTD script files	60
A.1	Infinitely long cylindrical nanowire	60
A.2	Diameter and dot height sweep to maximize transmission	61

A.2.1	Setup script	63
A.3	Gated InP nanowire with Al ₂ O ₃ dielectric cladding	63
A.3.1	Setup script	65
A.3.2	Analysis script	67
B	Python code	68
B.1	Circular two-dimensional Gaussian fit function	68
C	p-n junction cleanroom fabrication procedure	70
C.1	Mesa pattern	70
C.2	n-type ohmic contacts	72
C.3	p-type ohmic contacts	75
C.4	Oxide insulator and via-holes	76
C.5	Top gate and bond pads	77

List of Figures

2.1	Energy levels in a quantum dot	9
2.2	Biexciton-exciton cascade	10
2.3	Biexciton-exciton cascade with fine structure splitting	12
2.4	Four-gate configuration to apply a quadrupole electric field	13
2.5	GaAs/AlGaAs energy band diagrams showing flatbands and induced 2DEG and 2DHG for an undoped single heterojunction and quantum well.	16
2.6	Electron transport mobilities for a range of carrier densities in an undoped induced 2DEG and a modulation doped 2DEG	17
2.7	Landau level density of states in a two-dimensional carrier gas.	19
2.8	Pump mechanism of a single-parameter electron pump.	22
2.9	Spontaneous emission dynamics in an infinitely long nanowire	24
2.10	Micropillar cavity design	25
2.11	Adiabatic mode expansion in tapered nanowires	26
3.1	Tapered nanowire waveguide design	28
3.2	Lumerical FDTD model of tapered nanowire waveguide	29
3.3	Full spectrum of transmission efficiencies for varying nanowire diameter and quantum dot height.	30
3.4	$\eta \geq 95\%$ for varying nanowire diameter and quantum dot height.	31

3.5	Far-field emission profiles simulated using Lumerical FDTD.	32
3.6	Gated nanowire model	33
4.1	Device components of a p-n junction in an induced GaAs/AlGaAs heterostructure.	35
4.2	GaAs/AlGaAs heterostructure and mesa pattern	36
4.3	Fabricated n-type and p-type devices.	38
4.4	Device measurement setup	39
4.5	Magnetoresistance measurements of an induced 2DEG.	40
4.6	Magnetoresistance measurements of an induced 2DHG.	41
4.7	Top-gate voltage versus two-dimensional carrier densities for a 2DEG and 2DHG.	42
4.8	Density-mobility relationship for carriers in a 2DEG and 2DHG.	42
4.9	Ohmic behaviour of a 2DEG	43
4.10	Ohmic behaviour of a 2DHG	44
4.11	Picture of fabricated p-n junction diode along with I-V curves for three devices with different top-gate separations.	45
4.12	Diode behaviour of wide 2D p-n junction	46
5.1	GaAs/AlGaAs heterostructure with a quantum well.	49

List of Tables

3.1	Selected transmission efficiencies for different nanowire diameters and dot heights.	31
4.1	2DEG and contact resistances	43
4.2	2DHG and contact resistances	44

Chapter 1

Introduction

The study of the quantum nature of light and matter served as the basis for pioneering research by several scientists in the 20th century, yielding breakthroughs that completely revised our understanding of the physical world we live in, in turn resulting in revolutionary new technologies. Devices such as the transistor, photovoltaics and lasers arrived as part of the *first quantum revolution*, that directly arose from attempts to theoretically explain 19th and 20th century discoveries such as the photoelectric effect and black-body radiation. Since the start of the 21st century, a new class of technologies have been proposed and are being developed, ushering in a *second quantum revolution* [1]. These devices make use of our understanding of quantum superposition, entanglement and sensing to engineer unique quantum mechanical systems to possess favourable electronic and optical properties, and promise to revolutionize the fields of communication, imaging, metrology, remote-sensing and computing. However, there are many scientific and engineering challenges to overcome before such devices can be made practical. The aim of this thesis is to provide solutions to some of the challenges associated with the development of quantum light sources.

Section 1.1 offers some historical context to understand how these sources work and why they are useful. Section 1.2 describes the properties of an ideal quantum emitter, and evaluates the current state-of-the-art. Section 1.3 gives an overview of this thesis and a quick breakdown of each chapter.

1.1 Historical background

For a long time, it was believed that a *classical* picture was sufficient to explain all observable phenomena in nature. Max Planck was among the first scientists to challenge this notion through his formulation of a semi-classical model of light in 1900 [2] based on his analysis of black-body radiation. Black-body radiation is the thermal electromagnetic radiation emitted by an object, and possesses a wavelength and intensity dependent on the object's temperature [3]. Planck described this radiation as being emitted in discrete 'energy elements' whose value depended on the frequency of the emitting oscillator; this model explained experimental observations better than established classical descriptions of radiation. Until this discovery, it was assumed that light or in general electromagnetic radiation was wave-like in nature, as established by Thomas Young's famous double-slit experiment in 1801. Around the same time, Albert Einstein published his mathematical description of the photoelectric effect, a phenomenon demonstrating the dependence of the energy of light on its frequency as opposed to its intensity [4]. Einstein's formalism relied on quantizing *light itself* into individual particles. Each particle is generated and detected as a whole, and can propagate in free space independently; this model was consistent with Planck's hypothesis. These ground-breaking results gave rise to the concept of the elementary particle known as the *photon*, and firmly established the dual wave-particle nature of light.

It is now agreed that describing photons and other quantum objects in classical terms such as 'particle' or 'wave' is misleading, since these objects reside in their own separate category altogether. However, such descriptions offer a more intuitive understanding of the properties exhibited by photons. Quantum field theory (QFT) attempts to find a *true* understanding of the nature of photons and their interaction with matter, and is an active area of research. QFT formally defines a photon as an elementary excitation of a single mode of the quantized electromagnetic field [5]. Given a mode k with frequency ν_k of the quantized electromagnetic field, a single photon in this mode possesses an energy ϵ given by

$$\epsilon = h\nu_k, \tag{1.1}$$

where h is the Planck constant. An understanding of quantum light-matter interaction

forms the basis for the construction of sources and detectors of single photon states, and allow us to make use of the unique properties associated with these quantum objects.

In 1935, Einstein, Boris Podolsky and Nathan Rosen published a paper that outlined a strange effect arising from quantum mechanics [6]. Quantum theory predicts that certain quantum systems can become *strongly correlated*, such that their collective quantum state cannot be factored into a product of individual states. A paradoxical consequence of this is that when a measurement is conducted on a property of one system, it results in an instantaneous collapse of the collective state; thus the other systems in the collective ‘*know*’ that a measurement has been conducted even if the systems are arbitrarily far apart, implying that information can travel instantly. Erwin Schrödinger referred to such strong quantum correlations as quantum ‘entanglement’, with the states being ‘entangled’. This result, later dubbed the ‘EPR paradox’, seemed to indicate that quantum theory at the time was incomplete, and there were ‘hidden variables’ at play that linked entangled systems. The EPR paradox raised troubling philosophical questions regarding *locality* (the assumption that information cannot propagate instantly across an arbitrary distance) and *realism* (the assumption that the results of quantum mechanical measurements on a system arise from its real properties), and was the subject of several public debates between Einstein and the Danish physicist Niels Bohr. However, the hidden variable theory was disproved in 1964 by John Stewart Bell [7]. Bell’s theorem essentially drew a clear line between classical and quantum behaviour: *quantum properties cannot be explained using classical assumptions*. Since Bell’s startling discovery, entanglement has been successfully demonstrated in various quantum mechanical systems, and several experimental ‘Bell tests’ have been conducted to verify that local realism is insufficient to explain quantum mechanics [8]. Entangling photons via their *polarization states* is especially suited to this endeavour.

Quantum photonic devices are centred on the generation, manipulation and detection of single- and entangled-photons, and arrived with the second quantum revolution. In addition to pursuing answers to fundamental questions, these devices and their unique properties promise the development of: secure communication via *quantum key distribution* protocols such as the BB84 [9] or E91 [10] protocols; high-resolution *imaging* and *metrology* [11]; *remote-sensing* via quantum illumination [12]; *linear optical quantum computing* [13];

and *distributed quantum networks* (or a ‘quantum internet’) [14]. Three sub-categories of technologies have arisen: single-photon detectors, linear and nonlinear optical circuits, and single- (and entangled-) photon sources; the quantum light emitters described in this thesis belong to the final sub-category of devices.

1.2 The ideal quantum emitter

A quantum light source should possess certain properties [15, 16, 17, 18] to be classified as ideal, including:

- deterministic or on-demand photon generation - single photons generated in a predictable manner with 100% probability,
- single-photon purity - null probability of zero-photon or multi-photon emission,
- indistinguishability - all emitted photons indistinguishable from each other,
- high brightness - large number of photons emitted/collected per second,
- large *measured* entanglement fidelity - large degree of entanglement between two photons in an entangled pair as measured by sensitive photodetectors,
- position-controllability - the location of the source is possible to control, and
- coherent and tunable emissions - emission waveforms from different sources made identical.

Broadly, sources of single- and entangled-photon states can be divided into two categories: *probabilistic* and *deterministic* [15]. Single-photon sources based on spontaneous parametric down-conversion (SPDC) currently represent among the best and most widely-used sources, possessing entanglement fidelities of $\sim 97\%$ and source efficiencies of $\sim 5\%$ [19]. While their emissions have very high single-photon purity and indistinguishability, these sources are inherently non-deterministic (or probabilistic). Probabilistic single-photon sources rely on correlated photon pair emissions: the detection of one photon in the pair is used to ‘herald’ the emission of the other. This drastically reduces the number of ‘useful’ photons emitted. Additionally, since their purity and entanglement fidelity deteriorate with increasing brightness due to multi-photon emission, their brightness must be limited. These sources are thus restricted from certain applications such as remote sensing, which

requires bright, on-demand sources. Deterministic single-emitter sources such as quantum dots have therefore been the focus of intense research in the past decade.

Various material systems have been used to develop deterministic sources, including single atoms/ions [20, 21], ensembles of atoms [22], colour centres in crystals [23], quantum wells [24] and quantum dots [25, 26]. Of these, semiconductor quantum dots possess the largest purities (in excess of 99% [26]) and very high indistinguishabilities (> 92% [18]). Quantum dots are also capable of producing entangled photon pairs via a radiative cascade process (section 2.1.1). While these sources are theoretically deterministic, losses in the extraction of emitted photons (low brightness) and degradation of detected entanglement (low fidelity) effectively result in probabilistic implementations. Current research on deterministic sources aims to improve photon collection rates and detected entanglement fidelities.

In this thesis, two kinds of on-demand sources are discussed: quantum dots embedded in tapered nanowire waveguides (driven optically), and two-dimensional charge carrier gases confined in mesoscopic quantum wells (driven electrically), both implemented in III-V semiconductor systems.

1.3 Thesis overview

At the Quantum Photonic Devices (QPD) lab¹ in the Institute for Quantum Computing (IQC), our goal is to develop the next generation of solid-state quantum emitters and detectors for the advancement of quantum information and quantum communication technologies, while simultaneously seeking answers to fundamental questions in quantum optics. The work described in this thesis aims to contribute to the body of collective knowledge required to reach this goal.

Chapter 2 covers how deterministic single- and entangled-photon generation can be achieved in two classes of sources: optically-driven quantum dots and electrically-driven two-dimensional carrier gases in quantum wells. Techniques to engineer the environment

¹<https://uwaterloo.ca/institute-for-quantum-computing/research/groups/quantum-photonic-devices-lab>

surrounding the sources in order to boost their efficiency, shape their emission profiles and direct their emissions will also be discussed.

Chapter 3 examines the simulation results from a model to optimize the emission parameters of a tapered nanowire quantum dot source. Different architectural parameters are considered, with a suggestion of what best parameters to use when fabricating subsequent devices. Related code is included in appendices A and B. All results in this section were obtained by the author.

Finally, chapter 4 details the design and testing of a prototype device fabricated in-house that aids in the development of a new class of electrically-driven quantum emitter. The cleanroom fabrication steps for this device are given in appendix C. This project is conducted in collaboration with the Coherent Spintronics group² led by Prof. Jonathan Baugh, also at the IQC, and the Molecular Beam Epitaxy research group³, led by Prof. Zbigniew Wasilewski at the Waterloo Institute for Nanotechnology (WIN).

²<https://uwaterloo.ca/institute-for-quantum-computing/research/groups/coherent-spintronics-group>

³<https://uwaterloo.ca/molecular-beam-epitaxy>

Chapter 2

Bright, deterministic quantum light generation

As detailed in the introduction, ideal sources of single- and entangled-photons are deterministic (or on-demand), i.e. they predictably emit one photon at a time with a probability of 100% for each emission event. In other words, the event of ‘pulling a trigger’ results in the emission of *exactly one* photon, not more, not less. SPDC sources are inherently non-deterministic, and while they possess high purities and indistinguishabilities, their brightness is limited, restricting their potential applications.

Sections 2.1 and 2.2 cover the theory behind the emission of photons from two types of deterministic sources that can in theory be engineered to be very bright: optically driven semiconductor quantum dots and electrically driven quantum light sources. Section 2.3 explains ways in which the environment surrounding the emitters can be engineered to enhance the source brightness and collection efficiency, shape the profile of the emission in the far-field, and funnel the emissions along a specific direction.

2.1 Optically-driven semiconductor quantum dots

Quantum dots are a class of nanomaterial that possess unique optical and electronic properties by virtue of their small sizes. Solid-state quantum dots are capable of strongly confining electrons and holes, and are referred to as artificial atoms since they possess discretized energy levels that charge carriers can move between through exchanges of energy. The size and structure of quantum dots can be easily modified to reflect a change in their properties, making them an attractive candidate for the development of optical sources for quantum information and communication. They also possess the advantage of scalability and integration since they are compatible with existing semiconductor technologies.

Solid-state quantum dots are fabricated using epitaxial growth techniques. A variety of III-V semiconductor materials have been used to fabricate high-performing quantum dot sources, such as InAs/GaAs [27] and InP/InAsP [28], the latter being the material system of the sources used in the QPD group. Growth techniques that allow for the control of quantum dot size, shape and positioning possess a competitive advantage.

Both single photons and entangled photon pairs can be emitted from quantum dot sources through a radiative cascade process known as the biexciton-exciton cascade (section 2.1.1). The measured entanglement fidelity may be compromised due to strain in or around the quantum dot or asymmetry in its shape or charge environment, but this is possible to correct for (section 2.1.2). Because the photons from these sources propagate in all directions, there is a need to engineer the environment surrounding the source to funnel the emissions in one direction, as well as shape their mode while simultaneously enhancing the spontaneous emission rate of the source (section 2.3).

2.1.1 The biexciton-exciton cascade

Due to the strong quantum confinement of both valence- and conduction-band carrier wavefunctions, quantum dots possess atom-like discretized energy levels. Multiple excitations can occur across these energy states, resulting in unique emission properties. In epitaxially grown solid-state dots, there normally exist two confined shells per band, the n- and p-shell (figure 2.1). The wetting layer (the first atomic layer grown during

epitaxy) possesses a quasi-continuum of delocalized states that exist in the same energy domain as the localized shells in the dot [29]. When the system is placed at extremely low temperatures ($< 5\text{K}$) and excited off-resonantly (i.e. with an energy greater than the bandgap of the quantum dot) by a pump laser, free carriers (electrons and holes) are generated in the wetting layer that quickly relax into the lower energy shell states of the dot. (*Note:* low temperatures are required to prevent re-excitations of electrons between the energy levels).

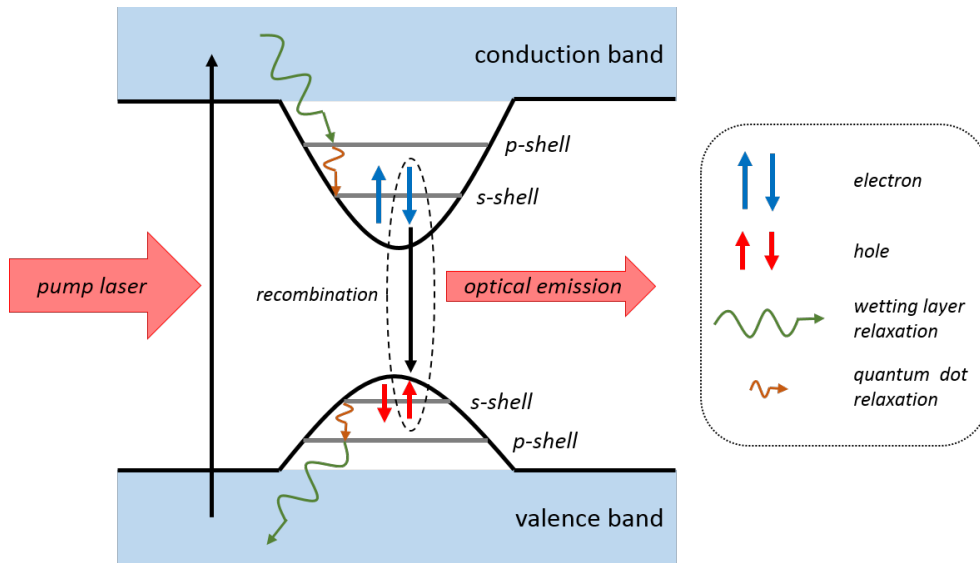


Figure 2.1: Energy states in a semiconductor quantum dot. Two shells are confined in the quantum harmonic potential of the dot. The quasi-continuum of states in the wetting layer are represented by the blue regions

The electron-hole pairs generated through this population inversion are called excitons. When the first electron-hole pair recombines, the resulting emission is called the biexciton (XX) emission, while the subsequent recombination yields the exciton (X) emission. This radiative recombination process is termed the biexciton-exciton cascade (figure 2.2), and was first presented as a means to produce entangled photon pairs using solid-state quantum dot emitters by Oliver Benson et. al. in 2000 [30].

The polarization states of the XX and X emissions depend on the spin states of the

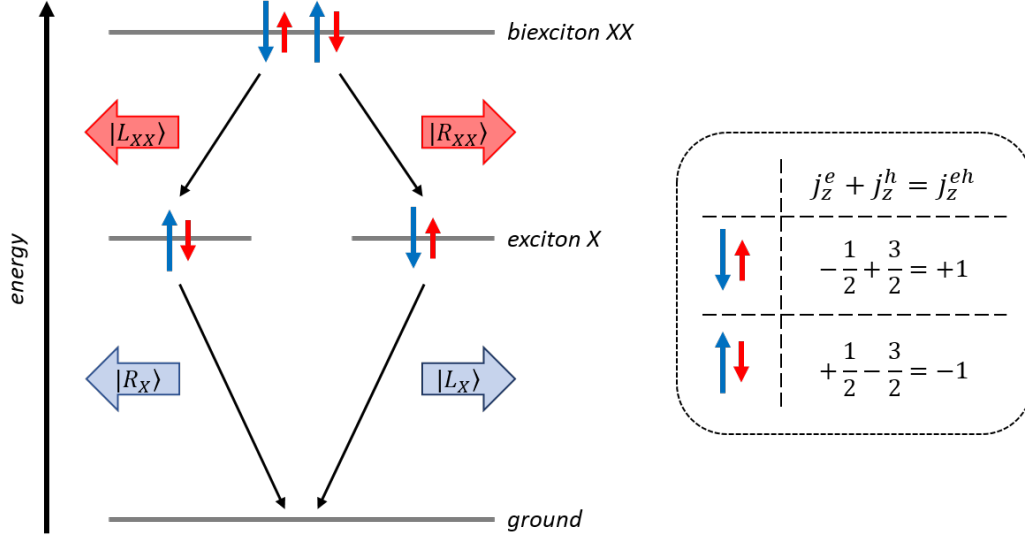


Figure 2.2: The biexciton-exciton radiative cascade for an ideal quantum dot. The X levels for the two recombination pathways are degenerate. Optical emission occurs when $j_z^{eh} = \pm 1$. The entangled output state is given by equation 2.1.

electron and hole in the recombining electron-hole pair [31]. The z-projection (j_z) of the total angular momentum quantum number (j) takes the values $+\frac{1}{2}$ (\uparrow) and $-\frac{1}{2}$ (\downarrow) for electrons in the conduction band. In lens-shaped dots with strong z-confinement, mostly heavy holes (and not light holes) are confined in the valence band, and j_z can equal $+\frac{3}{2}$ (\uparrow) or $-\frac{3}{2}$ (\downarrow) [32]. Recombination can occur between any pair of electron and hole, but an optical emission occurs only when the total angular momentum of the recombining electron-hole pair is ± 1 ; i.e. $j_z^e = -\frac{1}{2}$, $j_z^h = +\frac{3}{2}$ ($\downarrow\uparrow$) **or** $j_z^e = +\frac{1}{2}$, $j_z^h = -\frac{3}{2}$ ($\uparrow\downarrow$). A quantum dot initialized to the XX state can thus emit photons in two possible ways depending on which electron-hole pair recombines first: right circularly polarized XX emission ($|R_{XX}\rangle$) followed by left circularly polarized X emission ($|L_X\rangle$), or vice-versa. Ideally, the two X levels along each recombination pathway are degenerate, resulting in the maximally entangled two-photon Bell state

$$|\Psi\rangle = \frac{1}{\sqrt{2}}(|R_{XX}\rangle |L_X\rangle + |L_{XX}\rangle |R_X\rangle). \quad (2.1)$$

$|\Psi\rangle$ is rewritten in the horizontal (H) and vertical (V) polarization basis using the transfor-

mations

$$|H\rangle = \frac{1}{\sqrt{2}}(|R\rangle + |L\rangle); \quad (2.2a)$$

$$|V\rangle = \frac{i}{\sqrt{2}}(|R\rangle - |L\rangle), \quad (2.2b)$$

yielding

$$|\Psi\rangle = \frac{1}{\sqrt{2}}(|H_{XX}\rangle |H_X\rangle + |V_{XX}\rangle |V_X\rangle). \quad (2.3)$$

The entanglement fidelity of the measured two-photon state is given by

$$f = \text{Tr}[\rho' \cdot \rho_0], \quad (2.4)$$

where ρ' is the experimentally obtained density matrix reconstructed from cross-correlation measurements between the XX and X photons and $\rho_0 = |\Psi\rangle \langle\Psi|$ is the density matrix of the maximally entangled Bell state from equation 2.3. $\rho' = \rho_0$ for an ideal dot, and thus $f = 1$.

In practical implementations, there is an asymmetry in the recombination pathways of the XX-X cascade due to an energy splitting δ of the bright excitonic state, known as the fine structure splitting (FSS) (figure 2.3). This break in X degeneracy is because of the Coulombic exchange interaction coupling the electron and hole spins [33], which in turn can be due to several reasons, including elongation in the quantum dot shape [31], random alloying [34], or lattice strain [35]. The FSS causes a spin-orbit interaction that mixes the excitonic states, resulting in the eigenfunctions $\frac{1}{\sqrt{2}}(|\downarrow\uparrow\rangle - |\uparrow\downarrow\rangle)$ and $\frac{1}{\sqrt{2}}(|\downarrow\uparrow\rangle + |\uparrow\downarrow\rangle)$ [36]. During the cascade, the exciton precesses between these two states, modifying the output state in the HV basis to become time-dependent:

$$|\Psi(t, \delta)\rangle = \frac{1}{\sqrt{2}}(|H_{XX}\rangle |H_X\rangle + e^{-i\frac{\delta}{\hbar}t} |V_{XX}\rangle |V_X\rangle). \quad (2.5)$$

If the timing resolution τ of the measurement system is good enough ($\tau \ll \hbar/\delta$), the fidelity of the detected entanglement will not be degraded since precise energy detection is no longer possible (by the uncertainty relation $\Delta E \cdot \tau \geq \hbar/2$) [37]. However, detection systems are normally not fast enough to prevent this, causing $f < 1$. Section 2.1.2 discusses ways to erase the FSS and improve the measured entanglement of the output state.

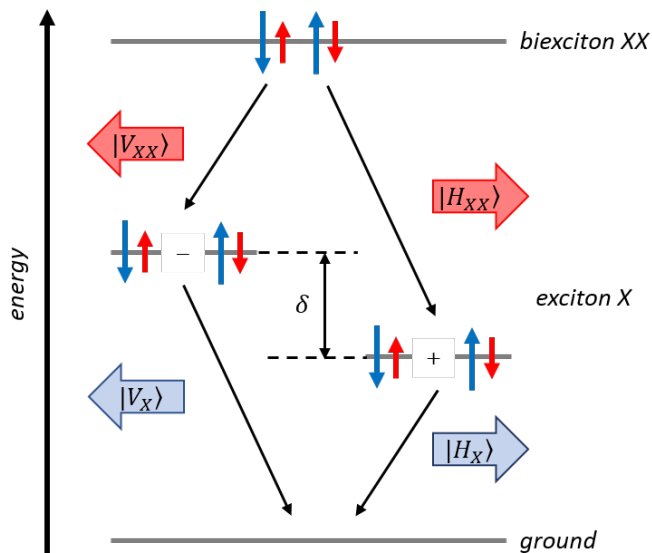


Figure 2.3: The biexciton-exciton cascade for a dot with fine structure splitting δ . The output state is given by equation 2.5.

2.1.2 Erasure of fine structure splitting

Several methods have been developed to remove FSS from quantum dots and improve the measured entanglement fidelity of the output state. Growth techniques producing symmetric dots have shown some promise [38, 39, 40], but are material specific and do not have a high yield. In addition, even dots with cylindrical symmetries have been found to possess FSS [32]. Post-growth perturbation using external electric fields [41], magnetic fields [42] and strain fields [43] can be applied to quantum dot sources regardless of the semiconductor material system, and can correct for varying levels of FSS. While strain-based tuning has proven to be quite versatile [25], it cannot be used on sources embedded in collection structures since the applied strain relaxes over a length scale of ~ 100 nm [44]. Collection structures are necessary to improve the light extraction efficiency and near-unity single mode fibre coupling of the emissions; the chosen FSS tuning technique must minimize FSS without compromising on source brightness. In July 2018, Fognini et. al. proposed an all-optical approach to eliminating FSS, preventing the need for additional fabrication [45]; this scheme requires specialized optical elements and electronics.

A model for the electron-hole exchange that causes the FSS (δ) in laterally deformed lens-shaped dots by Ramirez et. al. in 2010 derives the following relation:

$$\delta = \frac{2.K.\beta.\xi(1-\xi)}{(l_y^{eh})^3}, \quad (2.6)$$

where the factor $K = \frac{3\sqrt{\pi}e^2\hbar^2 E_p}{(4\pi\epsilon_0)16\sqrt{2}\epsilon m_0(E_g^b)^2}$ is in terms of physical constants and material parameters (E_p = conduction-valence band interaction energy, E_g^b = bulk energy gap, ϵ = dielectric constant), $\beta = |\langle \Psi_e | \Psi_h \rangle|^2$ is the electron-hole wavefunction overlap, and $\xi = \frac{l_y^{eh}}{l_x^{eh}}$ is a measure of the asymmetry in the exciton wavefunction (with $l_{x,y}^{eh}$ being the wavefunction extents). Minimizing β reduces δ , but compromises the source brightness by lowering the electron-hole recombination probability. The alternative is to tune ξ to 1 (or l_x^{eh} to equal l_y^{eh}) by applying an external electric field. Most works in this regard utilize a lateral field, but this requires a precise orientation relative to the dot dipole moment, and also lowers the brightness by reducing β . In September 2018, Zeeshan et. al proposed a novel FSS eraser using a quadrupole electric field [46]. This technique uses a system of four metal gates placed around and in the plane of a lens-shaped dot confined within a nanowire collection structure (figure 2.4). Using this configuration, it is possible to completely erase the FSS

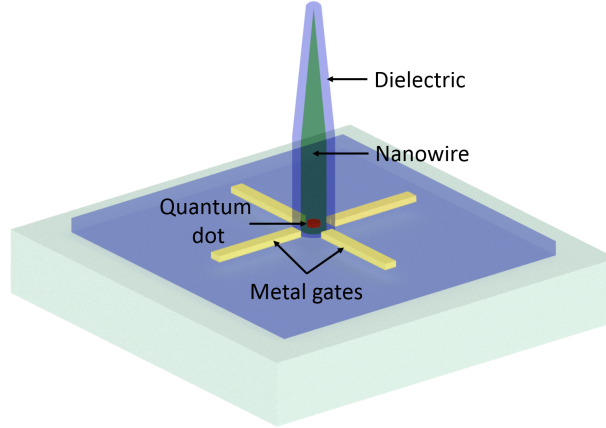


Figure 2.4: Quantum dot source inside a gated nanowire waveguide. The four metal gates apply a quadrupole electric field to erase the FSS.

for any dot dipole orientation while maintaining the source brightness and efficiency. The

Gaussian shape of the far-field emission from the tapered nanowire is also preserved; this is described in chapter 3.

2.2 Electrically-driven quantum light sources

The solid-state dot sources described in the previous section rely on optical excitations to achieve population inversion and subsequent quantum emission. A more practical approach that allows for scalability and increases emission rates is to integrate an electrical pumping mechanism to drive photon emission. Electron pumps (section 2.2.2) are generally implemented using two closely spaced tunable electric gates that create quantum confinement via tunnel barriers; by tuning their heights relative to each other, an integer number of charge carriers can be allowed to pass. A challenging aspect of this implementation is preventing electron-hole recombination at defect or impurity sites [18]; as such it is necessary to use defect-free materials with high carrier mobilities. Two-dimensional carrier gases induced in *intrinsic* high mobility III-V semiconductor quantum wells are an ideal candidate for such a material (section 2.2.1). Rectangular quantum well structures are created by sandwiching a sub-micron layer of *low-bandgap material* (such as GaAs) between layers of *high-bandgap material* (such as AlGaAs). Such layered heterostructure materials are fabricated using molecular beam epitaxy (MBE), which allows for precise control over the thickness and composition of each layer. High recombination probabilities and large emission rates require a high frequency pump transferring electrons from an electron-rich region to a hole-rich region, i.e. across lateral a p-n junction. Our goal is to implement a two-dimensional p-n junction in a quantum well structure with recombination controlled by a single-parameter electron pump; the design and testing of such a device is described in chapter 4.

2.2.1 Two-dimensional carrier systems

Tsuneya Ando et. al.'s 1982 review on the electronic properties of two-dimensional systems [47] serves as the primary reference for this section. Dynamically two-dimensional systems, in which charge carriers (electrons or holes) experience strong quantum confinement

along the z-direction but can freely move along the x- and y-directions, can be created through suitable doping [48] *or* by using the field effect [49] in layered semiconductor heterostructures. The field effect involves the application of an external electric field to modify the bandstructure of a semiconductor material, creating charge confinement that allows for carrier conduction by bending the bands below the Fermi energy at layer interfaces (figure 2.5). Such a field can be applied using a top-gate separated from the semiconductor surface by an oxide insulator. The two-dimensional confinement of electrons and holes, resulting respectively in a two-dimensional electron gas (2DEG) and two-dimensional hole gas (2DHG), can be induced at the interface of an undoped (intrinsic) *single heterojunction* (figures 2.5c and 2.5e) as well as within an intrinsic *quantum well* (figures 2.5d and 2.5f) by the applied top-gate voltage V_{TG} . Changing the polarity of V_{TG} changes the polarity of the induced carrier gas. Note that in either case, the magnitude of V_{TG} must exceed a threshold value before the confinement of electrons or holes begins and the 2DEG/2DHG is formed. The shape of the confinement potential at a single heterojunction interface is triangular, and is rectangular in a quantum well. Unlike doped samples, low-density 2DEGs and 2DHGs induced in intrinsic heterostructures via the field effect do not suffer from reduced conduction and carrier mobilities due to scattering from remote ionized impurities. Figure 2.6 (source: Harrell et. al. [49]) shows the improved mobility of induced intrinsic devices at low carrier densities compared to doped devices.

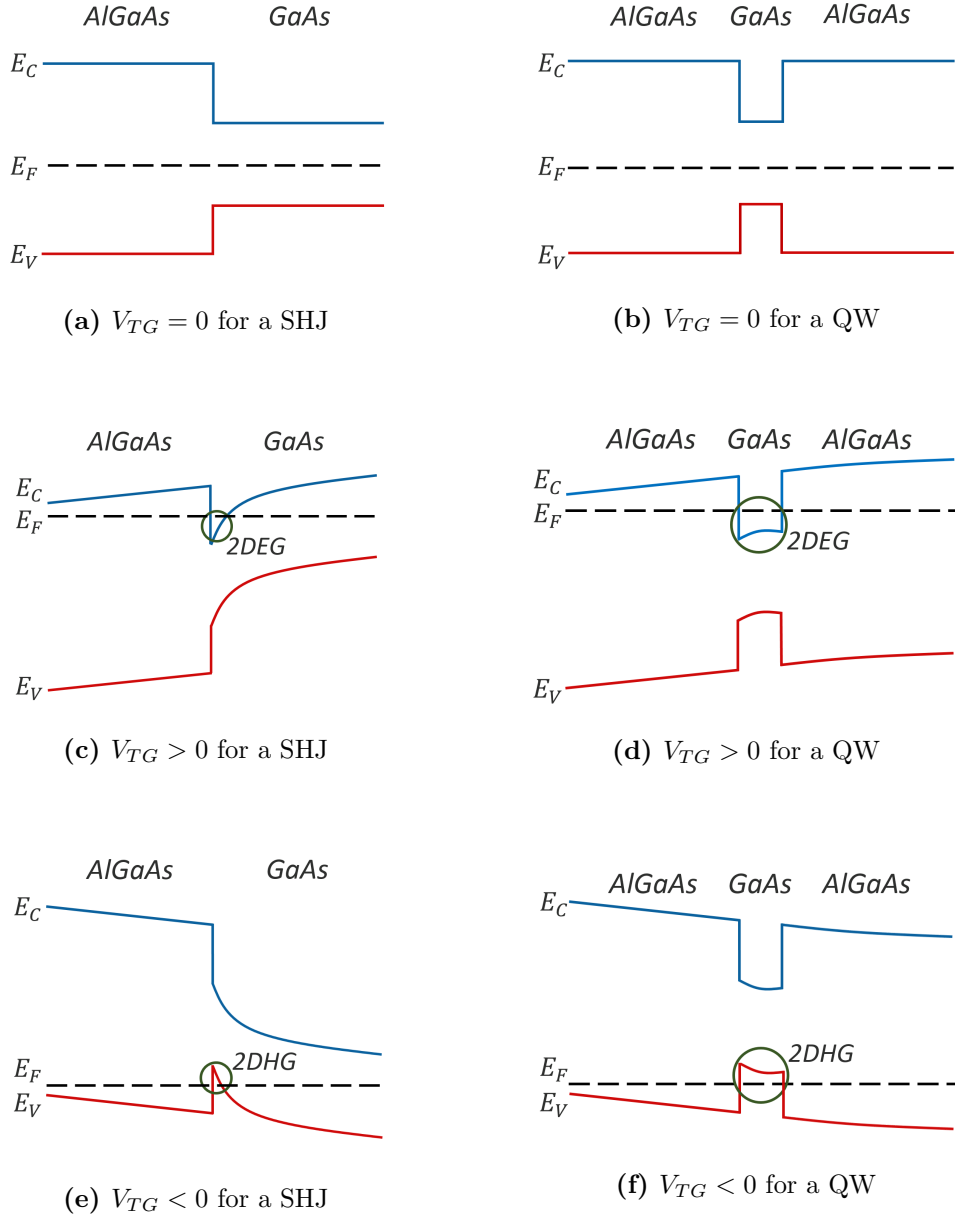


Figure 2.5: Energy band diagrams for undoped GaAs/AlGaAs single heterojunction (SHJ) and quantum well (QW) structures. The axes for each figure represent z -position (horizontal) and energy (vertical). To the left of each structure is a top-gate separated from the surface by an oxide, while the bulk substrate extends to the right. The conduction band E_C , valence band E_V and Fermi energy (E_F) are represented respectively by blue, red and dashed black lines. (a, b) No carrier gases induced, (c, d) 2DEG induced, (e, f) 2DHG induced.

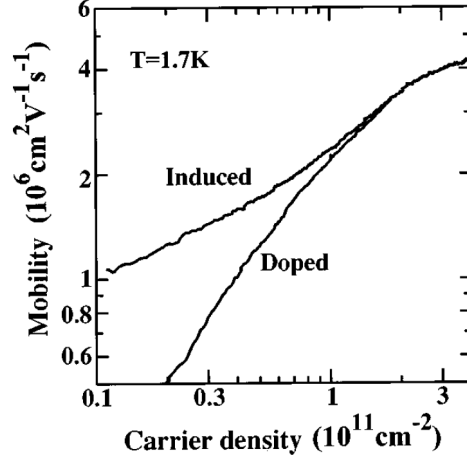


Figure 2.6: Electron transport mobilities for a range of carrier densities in an undoped induced 2DEG and a modulation doped 2DEG at 1.7 K. At low carrier densities, the doped device has greatly reduced mobility relative to the induced device. Reprinted from [49], with the permission of AIP Publishing (copyright permission on page 50).

In a z-confined 2DEG, the electron energies are quantized in the z-direction into *subbands*. The energy of the n th subband is E_n^z , with the total energy given by

$$E = E_n^z + \frac{\hbar^2}{2m_e^*}(k_x^2 + k_y^2), \quad (2.7)$$

where m_e^* is the effective mass of an electron and k_x, k_y are the components of the electron wavevector for motion in the plane of confinement. An effective way to validate the existence of a 2DEG/2DHG in an induced device is to measure its electrical properties under the application of an external magnetic field B directed perpendicular to its surface (z-direction).

This external B -field quantizes the carrier energies in the x-y plane in addition to the already existing z-quantization, creating Landau levels. Equation 2.7 then becomes

$$E = E_n^z + \frac{\hbar^2 k_l^2}{2m_e^*} = E_n^z + (l + \frac{1}{2})\hbar\omega_c, \quad (2.8)$$

where k_l is the wavevector of the l th Landau level and $\omega_c = eB/m_e^*$ is the cyclotron frequency of the electron. The Landau level density of states $g(E)$ are ideally delta functions (figure

2.7a). In reality, however, there is an energy broadening δE at each level due to electron scattering caused by impurities and defect sites, implying that Landau quantization will only be observable for $\hbar\omega_c \gg \delta E$. Assuming this condition is true, the number of occupiable states per unit area per Landau level is given by $2eB/h$, where the factor 2 accounts for spin. Each Landau level can further be treated as two spin-split half Landau levels, making the total energy

$$E = E_n^z + \left(l + \frac{1}{2}\right) \frac{\hbar e B}{m_e^*} \pm g^* \mu_B B, \quad (2.9)$$

where μ_B is the Bohr magneton, g^* is the effective g-factor, and the \pm accounts for spin-up and spin-down configurations. The two-dimensional carrier density n_{2D} is then

$$n_{2D} = \nu \frac{eB}{h}, \quad (2.10)$$

where the fill factor ν is the number of occupied spin-split half-Landau levels. Thus, the number of electrons per level *and* the spacing between consecutive levels are both affected by a changing magnetic field, in turn changing the conductance properties of the 2DEG. Consider the situation where the Landau Fermi energy E_F^l is at the middle of the highest occupied Landau level, i.e., ν is a half-integer (figure 2.7b). The system will have a high conductivity since there are a lot of empty states just above the Fermi energy that the electrons can enter. If E_F^l is between two levels, the highest occupied level is completely filled (i.e. ν is an integer), and the system acts as an insulator (figure 2.7c). It follows that sweeping the magnetic field switches the system between these two states, causing oscillations in the conductivity of the 2DEG. These oscillations are known as Shubnikov-de Haas oscillations. (*Note:* The magnitude of the *spin-splitting* between two half-Landau levels is much smaller than the *subband spacing* between Landau levels. Dips in conductivity are thus harder to observe in the case of the former due to the requirement of a high B -field.)

Another important phenomenon used to prove the existence of a two-dimensional electron (hole) gas is the integer quantum Hall effect. The *classical* Hall voltage V_{xy} is the voltage measured perpendicular to the direction of carrier conduction induced by a longitudinal voltage V_{xx} in a 2DEG or 2DHG. For a current I , the classical Hall resistance

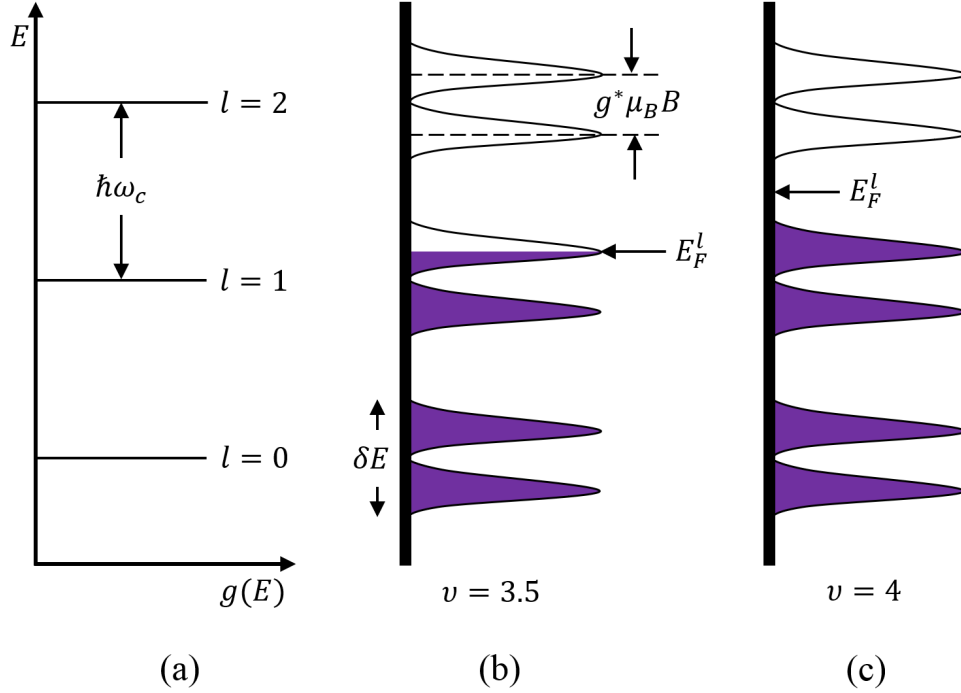


Figure 2.7: Landau level density of states created by quantizing a horizontal two-dimensional carrier gas with a vertically applied magnetic field. (a) $\delta E = 0$; (b) $\delta E \neq 0, \nu = \text{half-integer}$; (c) $\delta E \neq 0, \nu = \text{integer}$.

$R_H = V_{xy}/I$ is related to the two-dimensional carrier density n_{2D} as

$$R_H = \frac{B}{en_{2D}}, \quad (2.11)$$

where B is applied in the z -direction as before. At high values of B , R_H exhibits quantized plateaus [50] at values

$$R_H = \frac{1}{\nu} \left(\frac{h}{e^2} \right) = \frac{25.818}{\nu} k\Omega. \quad (2.12)$$

Here, only the *integer* values of ν are considered, corresponding to the number of *fully-occupied* spin-split half-Landau levels. The observation of these *quantum* Hall plateaus along with the Shubnikov-de Haas oscillations is used to validate the existence of a two-dimensional electron (hole) gas.

By measuring the hall resistance R_H , the two-dimensional electron (hole) density n_{2D} can be calculated using equation 2.11. The carrier mobility μ can be calculated in turn:

$$\mu = \frac{1}{n_{2D}e\rho_{xx}} \quad (2.13)$$

where

$$\rho_{xx} = \frac{V_{xx}|_{B=0}}{I(l/w)}. \quad (2.14)$$

Here, l and w are the length and width of the electron gas region. Note that the above results can be applied to holes confined in 2DHGs as well; m_e^* is replaced by the effective hole mass m_h^* .

The most important advantage of using the field effect in an undoped device over a doped sample is the ability to simultaneously induce a 2DEG and a 2DHG in the same GaAs/AlGaAs heterostructure via a split top-gate. By inducing these electron and hole gases next to each other and contacting them with ohmic contacts, a bright source of photons via electron-hole recombinations can be created. Deterministic integer photon generation can be subsequently engineered by adding Schottky gates to the device to create an on-demand single electron pump.

2.2.2 Single-parameter electron pumps

The need to individually manipulate single quantized charges originated with metrological experiments designed to redefine the ampere and other electrical standards [51, 52]. All single charge manipulation techniques involve the use of two potential barriers in an otherwise conductive region applied by a pair of closely spaced electrical gates. Charges can be allowed to pass over or tunnel through these barriers depending on the heights of the barriers. By tuning the barrier heights with a frequency f , charges can be made to pass individually, creating a quantized current

$$I = nef, \quad (2.15)$$

where e is the electron charge and n is the number of electrons *pumped* across the barriers per tuning cycle. When designing these devices, the overall conductance must be optimized

such that it is low enough to suppress charge noise to keep n from fluctuating, but high enough to ensure the pump rate f is not compromised [53].

Single-parameter pumps [54, 55] work by tuning the height of the entrance tunnel barrier with an RF voltage while keeping the exit barrier height fixed above the Fermi level E_F (figure 2.8). Initially, the entrance barrier height is below E_F , allowing a relatively large number of charges to load (figure 2.8a). The barrier is then quickly raised, leading to an avalanche of back-tunneling of most charges (figure 2.8b). m charges are left trapped in the potential well (figure 2.8c), and n of them are subsequently ejected with unity probability once the entrance barrier reaches a high enough amplitude (figure 2.8d). The entrance gate controls the number of trapped charges m and can in turn affect an increase in n . The exit gate controls n but has no effect on m . The energy of the ejected electrons will be different depending on the height of the barriers relative to E_F .

By having to vary just one gate voltage, the problem of phase synchronization between different variable parameters does not arise. In addition, no external bias voltage is required to facilitate charge pumping; noise in this external bias that may otherwise cause fluctuations is therefore not a cause for concern. Single-parameter charge pumps are capable of operating at a frequency of over 1 GHz; integrating these charge sources into a two-dimensional p-n junction would yield very high photon emission rates. By increasing the number of pumped charges per cycle to two, correlated photon pair emission could also be achieved.

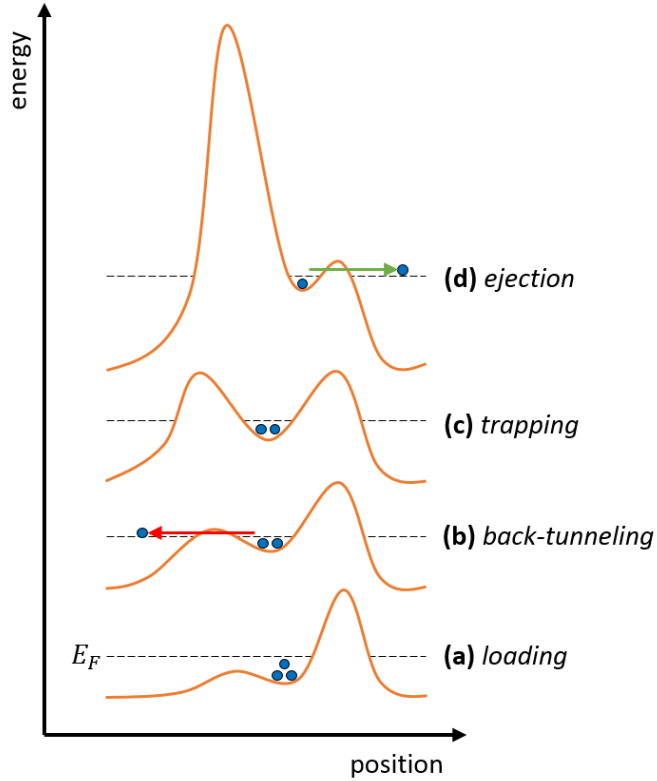


Figure 2.8: Pump mechanism of a single-parameter electron pump. Each pump cycle involves charge loading, back-tunneling, trapping and ejection. The entrance gate controls the barrier to the left, and the exit gate controls the barrier to the right. The Fermi level E_F is indicated by the dashed line.

2.3 Collection structures

Since the emissions from single-emitter sources propagate in all directions, there is a need to engineer the environment surrounding the source to funnel the emissions in one direction. For a majority of solid-state quantum dots, this is achieved using III-V semiconductor nanowire waveguides. These nanowires could be etched around pre-grown dots (*top-down* approach [56]) or the nanowire and dot can be grown in tandem (*bottom-up* approach [28]). While top-down nanowire sources possess high brightness (defined as the number of

photons arriving at the first collection optic), they are limited by defects due to the etching process. Controlling the dot position inside such nanowires is also challenging. Bottom-up growth, although resulting in less bright sources, allows for a more precise control of the dot position within the waveguide, and does not suffer from the same fabrication imperfections.

For the purpose of coupling the emission from a quantum dot into an optical fibre, restricting it to a single mode is necessary [57, 58]. In cylindrical waveguides, this mode is labelled the fundamental or HE_{11} mode [59]. For any given emitter, we are interested in maximizing the spontaneous emission rate Γ into the HE_{11} mode relative to the emission rate Γ' into higher-order guided modes, as well as the rate γ into the continuum of radiation modes (non-guided or ‘leaky’ modes). This is equivalent to maximizing the factor β given by

$$\beta = \frac{\Gamma}{\Gamma + \Gamma' + \gamma}. \quad (2.16)$$

The goal is thus to increase Γ while simultaneously reducing Γ' and γ . Γ is enhanced by the nanowire waveguide via the Purcell Effect [60], named for its discoverer Edward Mills Purcell. The level of Purcell enhancement of the HE_{11} emission by the nanowire is given by the Purcell factor F_p :

$$F_p = \frac{\Gamma}{\Gamma_0}, \quad (2.17)$$

where Γ_0 is the spontaneous emission rate of the dot in bulk semiconductor.

To lower Γ' and γ , emission into higher-order and radiation modes is restricted by setting upper and lower bounds to the waveguide diameter d , determined by analyzing the spontaneous emission dynamics of the nanowire (figure 2.9). In figure 2.9a, F_p peaks at $d/\lambda_e \approx 0.24$ (where λ_e is the free space emitter wavelength); this corresponds to the maximum Purcell enhancement of the HE_{11} mode [61]. Values above $d/\lambda_e \approx 0.35$ including the peak at $d/\lambda_e \approx 0.4$ are ignored since they correspond to the combination of HE_{11} spontaneous emission with the higher-order HE_{12} mode. This is in agreement with Claudon et. al.’s upper-bound of $d/\lambda_e = 0.366$ [62]. From figure 2.9b we deduce that γ is minimum in the range $0.23 \leq d/\lambda_e \leq 0.28$. This yields a β -factor of 90% within this diameter range.

The following subsections cover how the spontaneous emission and extraction efficiency can be further enhanced in finite nanowires, as well as how to shape the far-field emission profile to allow for single-mode fibre coupling.

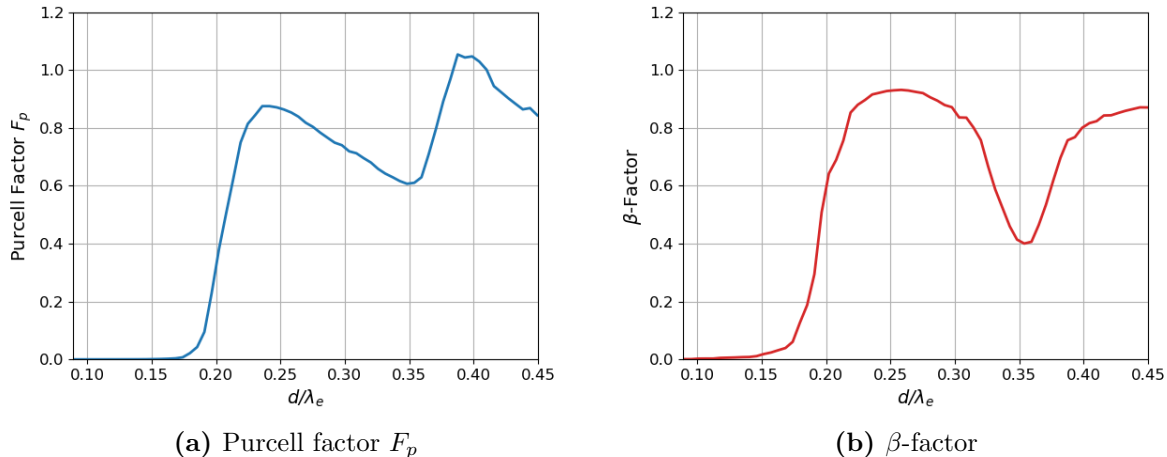


Figure 2.9: Spontaneous emission dynamics of a quantum dot in an infinitely long cylindrical nanowire waveguide. The dot is modelled as a linear dipole source located radially on the axis of the nanowire. F_p is maximum at $d/\lambda_e = 0.236$, while β is maximum at $d/\lambda_e = 0.258$. Lumerical script in section A.1.

2.3.1 Micropillar cavities

Placing a quantum dot source between two reflective surfaces creates a planar cavity that can be used to accelerate its rate of spontaneous emission into a certain mode (labelled the ‘cavity mode’) via the Purcell effect [63]. The cavity magnifies the local density of electromagnetic modes around the dot, driving F_p over unity and drastically enhancing emission brightness while simultaneously narrowing the linewidth. Micropillar cavities are fabricated by etching pillars around pre-grown dots sandwiched between two distributed Bragg reflector (DBR) layer stacks (figure 2.10). The upper mirror should have a transmission three times that of the lower to allow for efficient photon collection at the top [56]. Since the dots in the substrate may be randomly situated and possess varying emission properties, choosing the right dot to etch around is difficult. If the dot’s position is well defined and has an emission line in resonance with the cavity mode, the challenge is to centre the dot on the axis of the micropillar so that the emissions efficiently couple to the pillar waveguide mode [64]. In addition, sidewall roughness due to top-down

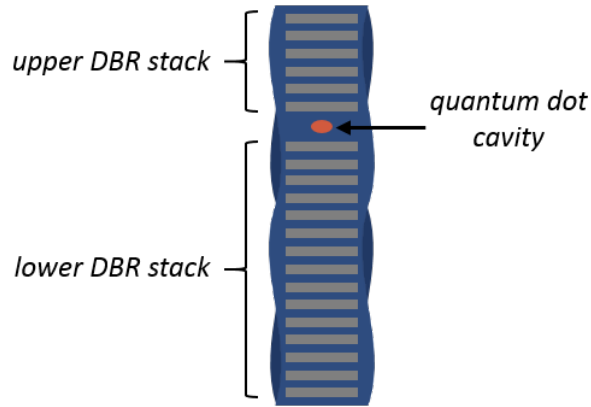
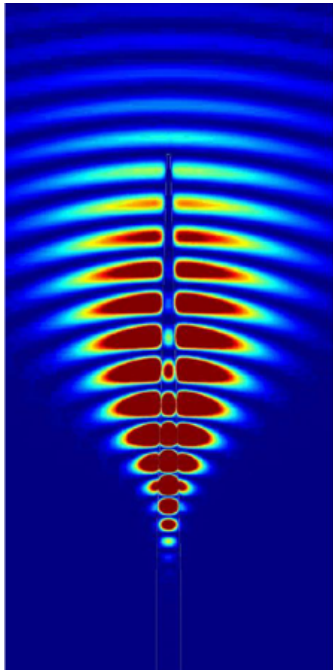


Figure 2.10: Semiconductor quantum dot inside a micropillar cavity. The cavity is asymmetric to allow for collection from the top. The sidewalls are rough due to fabrication imperfections.

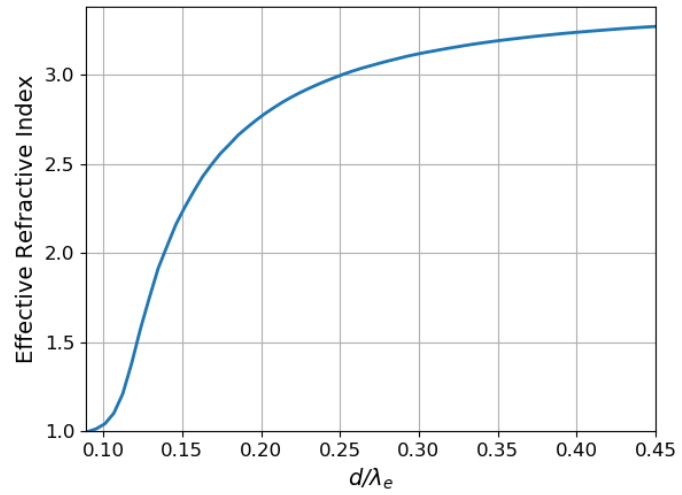
etching imperfections leads to losses in emission. Despite these challenges, sources using micropillar cavities still have the best brightness, though their emissions lack shaped modes for subsequent coupling to a single mode fibre.

2.3.2 Tapered nanowires

Bottom-up nanowire growth allows for the placement of a single quantum dot on the axis of the waveguide, increasing the coupling efficiency of the emitted mode with the waveguide. Nanowires grown epitaxially via the vapour-liquid-solid (VLS) method tended to have stacking faults around the dot [65], creating charge traps that induce multi-photon emission, but more recent work has corrected for this [66]. Another advantage of bottom-up growth is the ability to introduce a very sharp taper ($< 2^\circ$) at the top of the waveguide (compared to $\sim 5^\circ$ for top-down tapered waveguides [27]). This architecture prevents losses due to total-internal reflection at the semiconductor-air interface by achieving a smooth, adiabatic transition of the effective refractive index experienced by the outward propagating mode [61] (figure 2.11). Importantly, a sharp taper tailors the shape of the emission mode to a Gaussian in the far-field, increasing the coupling efficiency to a single mode optical fibre [57]. A numerical model of the quantum dot source inside a tapered nanowire waveguide is discussed in chapter 3.



(a) Simulated mode expansion



(b) Adiabatic conversion of effective refractive index

Figure 2.11: Adiabatic transition of the emitted mode in tapered nanowires

Chapter 3

Nanowire quantum dot source model

Since its inception, the QPD group has collaborated with scientists at the National Research Council (NRC) in Ottawa to design and fabricate semiconductor nanowire quantum dot sources for use in quantum optics experiments [67]. These sources are fabricated using a bottom-up VLS growth technique that ensures a single quantum dot (InAsP) is centred along the axis of a tapered nanowire (InP), maximizing the coupling between the emitted mode and the waveguide. The angle of the nanowire taper, the diameter of the nanowire, its cylindrical base height and the height of the dot from the bottom are all controllable parameters (figure 3.1). These parameters must be optimized to maximize the brightness of the source while maintaining a circular Gaussian emission profile in the far-field. In practice, the source transmission efficiency can be significantly boosted by coating the base of the nanowire with a mirror (usually gold), to reflect any downward propagating modes from the source back up and collect them along with the upward emissions [28]. Section 3.1 details the parameter optimization results of a nanowire quantum dot source model constructed using a commercially available Maxwell solver for nanophotonic devices based on the finite-difference time-domain (FDTD) method, called Lumerical FDTD.

It is also useful to model the emission properties of existing nanowire structures that have been modified by additional fabrication processes. Particularly, it must be ensured that the emissions from the gated nanowire waveguide described in section 2.1.2 are not significantly affected by the surrounding metal gates and the dielectric cladding. Section

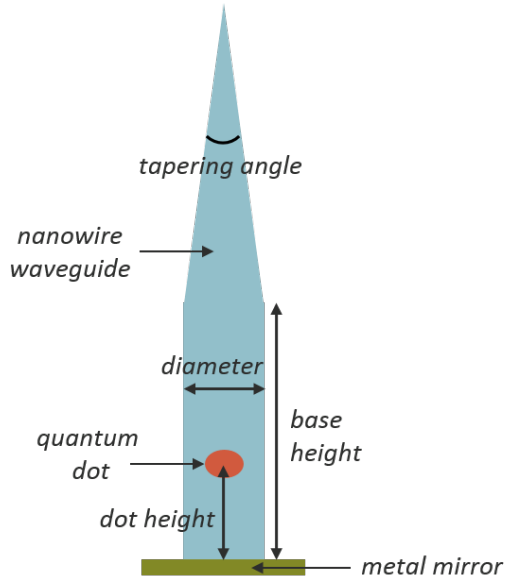


Figure 3.1: Schematic of a quantum dot source inside a tapered InP nanowire waveguide.

3.2 outlines the results of this model.

3.1 Parameter sweep to maximize brightness

While there are several controllable architectural parameters of the source, optimizing all of them through parameter sweeps is time consuming. However, the number of parameters to optimize are easily reduced through a few assumptions. Since the emissions from the source must possess a Gaussian far-field emission profile, a sharp nanowire taper of 2° is ideal. Additionally, at very low temperatures ($\sim 4K$), the extinction coefficient of the nanowire material (the imaginary part of its refractive index, indicating the level of attenuation on a propagating electromagnetic wave) is approximately zero, implying that the waveguiding properties of the nanowire are not affected by the height of the cylindrical base: i.e., the source brightness is not compromised more over longer distances since there is no attenuation; the cylindrical base height is thus set to a typical value of $1.5 \mu\text{m}$. With these simplifications, a source model is constructed using Lumerical FDTD to maximize

the *transmission efficiency* (η) at the end of the tapered nanowire by optimizing the *waveguide diameter* (d) and the *vertical position of the quantum dot* (z_{QD}) (figure 3.2). The quantum dot is modelled as a dipole point source located radially on the axis of an InP nanowire. The mirror at the bottom facet of the nanowire is implemented by modifying the simulation boundary condition to metallic at that location. The remaining boundaries of the three-dimensional simulation region are perfectly matched layers (PMLs) that strongly absorb any incident radiation, effectively acting as open boundaries.

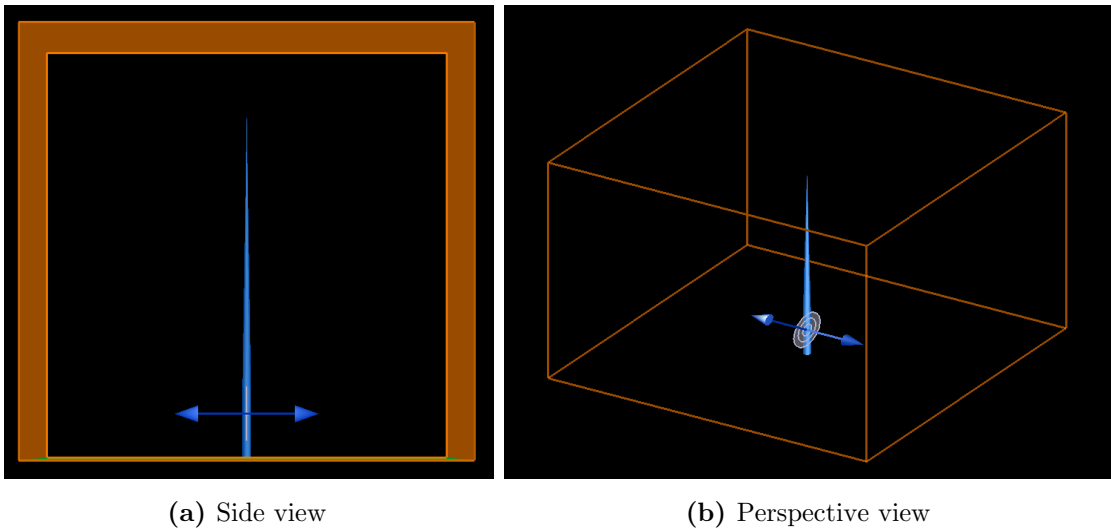


Figure 3.2: Quantum dot emitter modelled as a dipole source embedded in a nanowire with a 2° taper and $1.5 \mu\text{m}$ cylindrical base height. The bottom facet boundary condition is metallic, while the remaining boundaries are PMLs.

Based on the spontaneous emission dynamics of a dot in a nanowire described in section 2.3, the reduced diameter d/λ_e (λ_e is the emission wavelength) is varied from 0.23 to 0.28 (ensuring $\beta > 90\%$) in steps of 1 nm. The dot must be positioned in a manner that allows for the constructive interference of upward emissions with reflected downward emissions, i.e. it must be placed at an antinode of the emission electromagnetic field. z_{QD} is swept from $0.2 \mu\text{m}$ to $1.4 \mu\text{m}$ in steps of 50 nm to guarantee at least one antinode is covered. The results of this simulation are shown in figure 3.3. There are clearly defined regions in the parameter space ($d/\lambda_e, z_{QD}$) corresponding to constructive and destructive interference of

the emission electromagnetic field. The peak regions corresponding to $\eta > 90\%$ are broad, while the troughs ($\eta < 30\%$) are sharp. There is an overall trend of alternating peaks and troughs in the transmission for a fixed value of d/λ_e and varying z_{QD} .

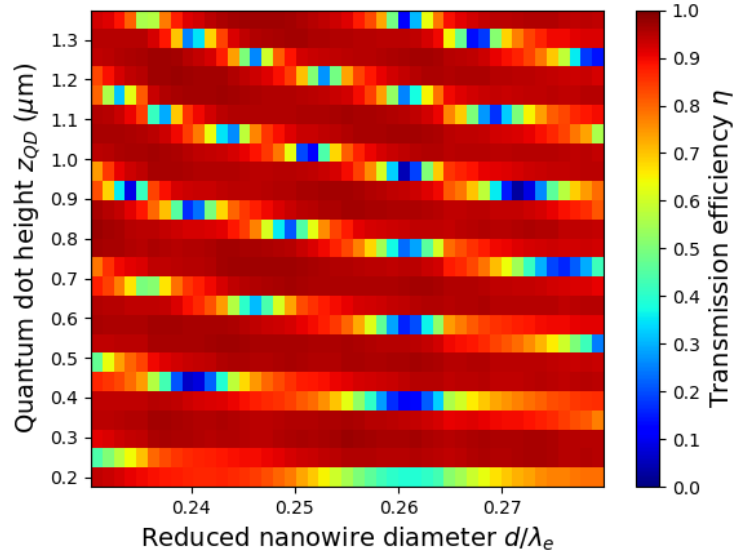


Figure 3.3: Full spectrum of transmission efficiencies for varying nanowire diameter and quantum dot height.

Figure 3.4 is a reproduction of figure 3.3 with $\eta > 95\%$ highlighted. The variation in the *spread* of high transmission domains across the parameter space indicates that certain values of dot height and nanowire diameter offer greater tolerance to error than others. The $(d/\lambda_e, z_{QD})$ pairing of $(\sim 0.237, \sim 1.275 \mu\text{m})$ yields the greatest flexibility in parameter values while maintaining η over 97%. The overall maximum value of η is also present in this domain, with a value of 97.32% at $(0.238, 1.25 \mu\text{m})$. Importantly, through correspondence with NRC, it was determined that the uncertainties in d/λ_e and z_{QD} during device fabrication are ± 0.011 and $\pm 50 \text{ nm}$ respectively. This makes the parameters corresponding to the transmission peak at $(0.248, 0.5 \mu\text{m})$ a better choice for maintaining a high transmission with a greater degree of flexibility. Table 3.1 lists the parameters corresponding to all the high transmission domains, as well as $\eta \sim 50\%$ and the lowest value of $\eta = 2.92\%$.

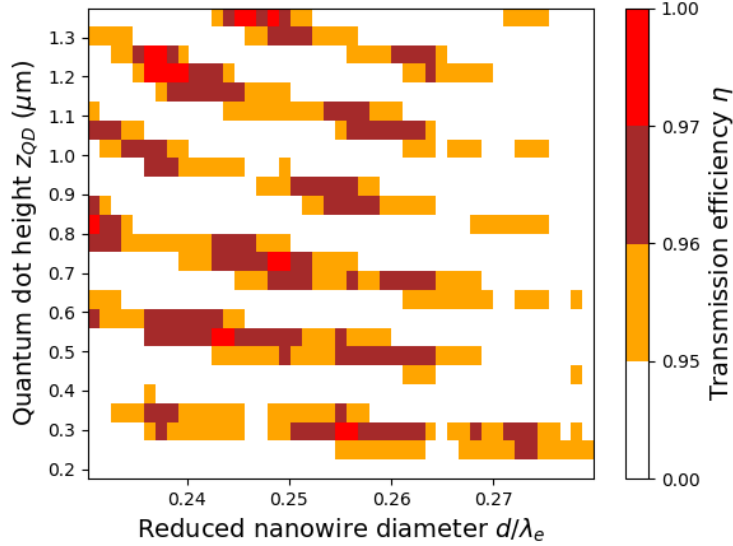


Figure 3.4: $\eta \geq 95\%$ for varying nanowire diameter and quantum dot height.

d/λ_e	z_{QD} (μm)	η (%)	R^2 Gaussian fit (%)
0.238	1.25	97.32	97.31
0.230	0.85	97.27	97.19
0.255	0.3	97.27	97.12
0.243	0.55	97.13	98.93
0.236	1.3	97.13	97.83
0.248	0.75	97.12	96.65
0.246	1.4	97.10	98.69
0.267	1.15	50.21	91.46
0.272	0.95	2.92	61.59

Table 3.1: Selected transmission efficiencies for different nanowire diameters and dot heights.

The fourth column in table 3.1 contains the R^2 goodness-of-fit values of the far-field emission profiles at these coordinates to two-dimensional Gaussian functions. Interestingly, the best Gaussian fit of 98.93% occurs at (0.243, 0.55 μm), which do not correspond to the parameters for highest transmission (0.238, 1.25 μm). This is explained by observing the far-field emission profiles for these two coordinates (figures 3.5a and 3.5b). The peak height

is larger for the latter, implying its improved Gaussian nature. Despite these differences, all high- η domains have far-field profiles with $R^2 > 96\%$. The far-field at $\eta = 50.21\%$ (figure 3.5c) has a relatively shrunken profile in k -space, and a reduced fit of 91.46%. R^2 is even lower (61.59%) for $\eta = 2.92\%$ (figure 3.5d), with the emission profile no longer resembling a Gaussian at all.

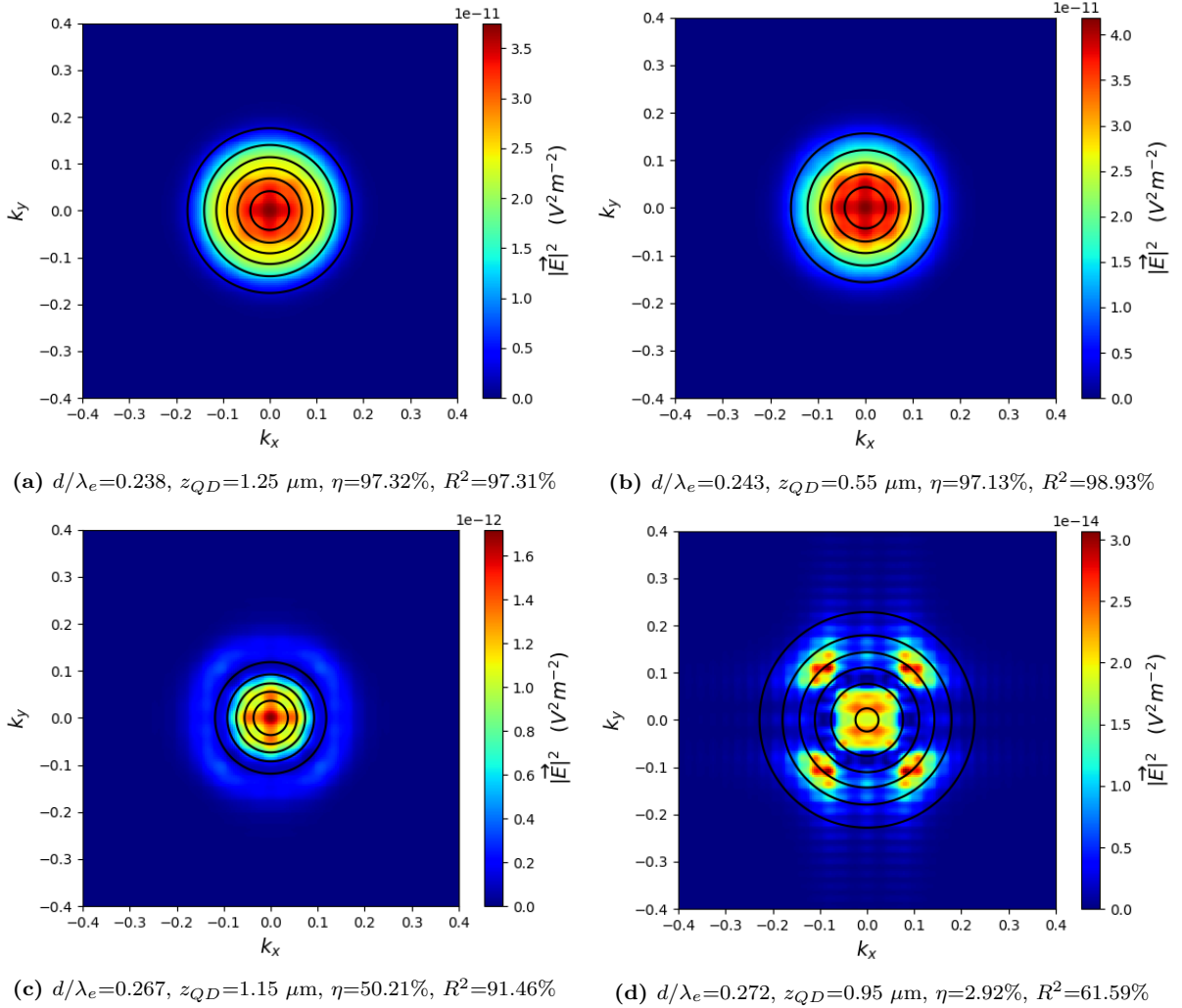


Figure 3.5: Far-field emission profiles simulated using Lumerical FDTD corresponding to (a) maximum η , (b) maximum R^2 , (c) $\sim 50\%$ η and (d) minimum η .

3.2 Gated nanowire quantum dot source

The nanowire quantum dot source described in section 2.1.2 is surrounded by four metallic gates for the purpose of applying a quadrupole electric field to erase the FSS. In addition, there exists a uniform cladding of Al_2O_3 dielectric, which due to current fabrication restrictions cannot be removed from the nanowire. It was of significant interest to determine whether the brightness and far-field emission profile of the source were compromised due to these additional surrounding features. Using a Lumerical FDTD source model defined in section A.3, the extraction efficiency and far-field emission profile of this source were obtained (figure 3.6). The device dimensions were set to match an existing gated source. The two-dimensional Gaussian fit of the far-field yielded an R^2 value of 97.85%. This near-unity overlap confirms that the metal gates do not modify the emission mode profile significantly. The light extraction efficiency is calculated to be 35.31%, which can be optimized further by removing the dielectric cladding, integrating a mirror at the base, and utilizing the optimized dot height and nanowire radius from section 3.1.

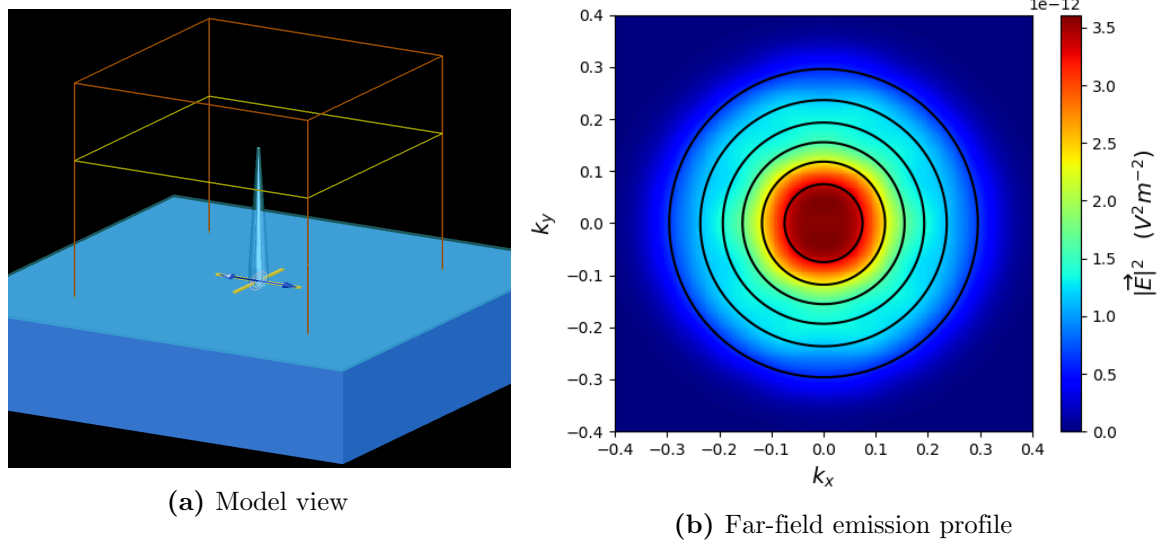


Figure 3.6: Lumerical model and resulting far-field emission profile for a gated nanowire structure. Calculated light extraction efficiency = 35.31%. The overlaid contour lines indicate a Gaussian fit of $R^2 = 97.85\%$.

Chapter 4

Design and testing of all-electric quantum emitter

Since September 2017, the QPD group has collaborated with the Coherent Spintronics group (CSG, led by Prof. Jonathan Baugh) and the Molecular Beam Epitaxy (MBE) research group (led by Prof. Zbigniew Wasilewski) on an ongoing project to develop an all-electric quantum emitter through the integration of a single-parameter electron pump and a wide two-dimensional p-n junction diode. The diode is created by inducing an embedded 2DEG and 2DHG adjacent to each other in a GaAs/AlGaAs heterostructure using a split top-gate and contacting these charge carriers with ohmic contacts. The device described in this chapter is one of the milestones achieved in the development of this p-n junction diode. The electron and hole gases are currently being induced at a GaAs/AlGaAs single heterojunction interface; future devices will utilize an induced 2DEG/2DHG in a quantum well, which will then be integrated with the electron pump.

All device fabrication was conducted at the Quantum-Nano Fabrication and Characterization Facility in the University of Waterloo, in collaboration with Dr. Francois Sfigakis and Brandon Buonacorsi from CSG. The GaAs/AlGaAs substrate wafers were grown by the MBE research group. The cleanroom fabrication recipe for the final p-n device is listed in appendix C. Section 4.1 details the architectural components of the device and how they come together. The existence of the induced electron and hole gases at cryogenic

temperatures was established using magnetoresistance measurements, and their ohmicity and carrier mobilities and densities were subsequently quantified (section 4.2). Finally, section 4.3 describes the p-n diode behaviour of the completed device.

4.1 Diode architecture

The important architectural components of the p-n junction device are shown in figure 4.1. Every feature is patterned using ultraviolet lithography techniques; positive and

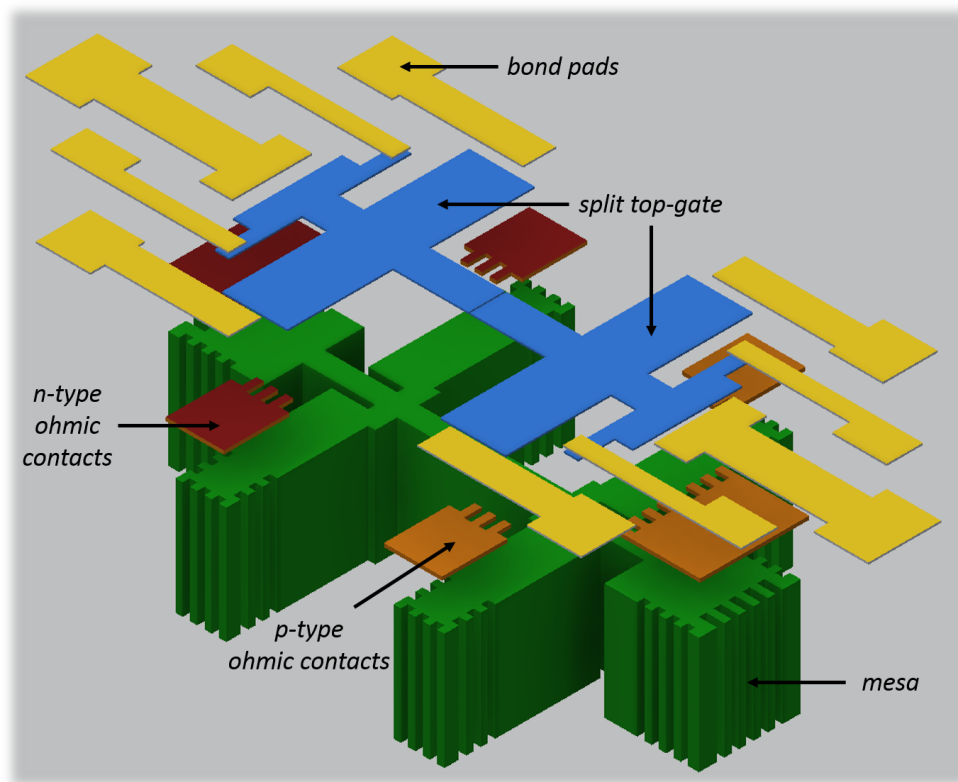


Figure 4.1: Device components of a p-n junction in an induced GaAs/AlGaAs heterostructure.

negative photoresists are both needed for different steps. The device is fabricated using a GaAs/Al_{0.3}Ga_{0.7}As heterostructure wafer grown using MBE. The single heterojunction

interface at which the 2DEG and 2DHG are induced is located 310 nm below the surface. An elevated area or mesa is patterned and etched into the substrate past this interface to define the region in which charge carriers can be induced and transported. Low-resistance ohmic contacts are then deposited to contact the 2DEG and 2DHG, which are induced by a pair of transparent top-gates separated by a narrow gap. The top gate and the bond pad leads are separated from the device by an oxide insulator with via holes to allow some leads to connect to the ohmic contacts.

4.1.1 Substrate wafer specifications and mesa

A schematic of the layered MBE-grown substrate wafer is shown in figure 4.2a. The wafer is capped with a 10 nm thick layer of GaAs to prevent oxidation of the relatively more reactive AlGaAs barrier layer. The AlGaAs thickness determines the depth of the single heterojunction and thus the 2DEG/2DHG. In this case the junction depth is chosen to be 310 nm since device fabrication is easier; future devices will use a shallower 2DEG to more easily implement the tunnel barriers of the electron pump. Figure 4.2b shows

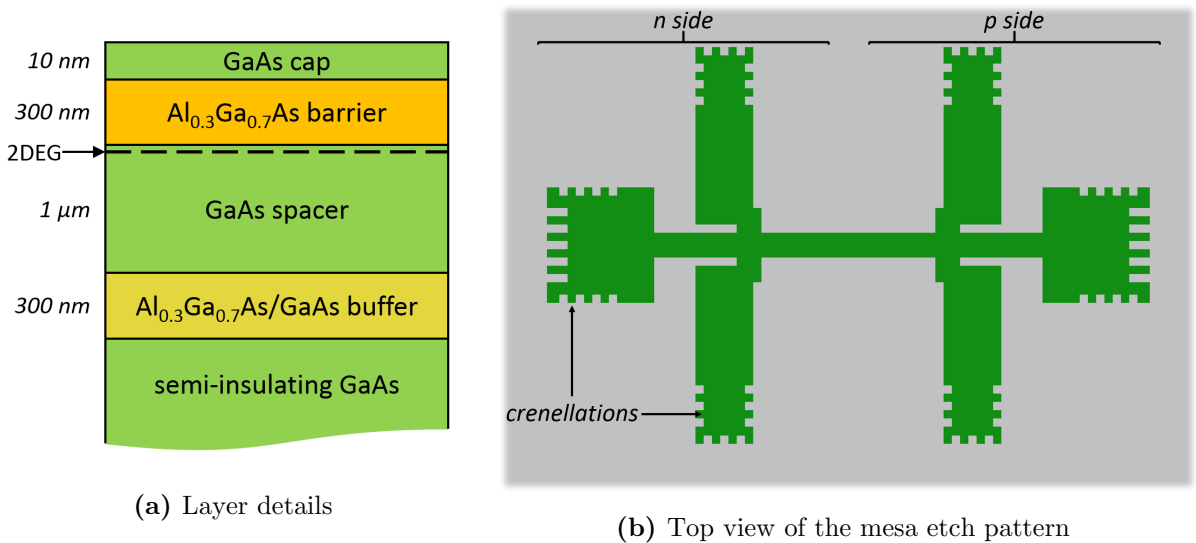


Figure 4.2: GaAs/AlGaAs heterostructure and mesa pattern

the pattern of the mesa etched into this wafer, which allows for three ohmic contacts on

each end of a wire: n-type on the left and p-type on the right. Both longitudinal and Hall measurements can be conducted with this configuration. The crenellations at the edges of the mesa increase the contact perimeter and decrease contact resistance between the ohmic contacts and 2DEG (2DHG). The height of the mesa must be over 310 nm to ensure that the electron or hole gas region is well-defined; the target etch depth is set to 350 nm.

4.1.2 Ohmic contacts

n-type and p-type alloyed ohmic contacts are required to form an electrical connection with the induced 2DEG and 2DHG respectively. A recess or pit is etched into the edges of the mesa before the contacts are deposited. n-type contacts are fabricated by depositing (10/250/120) nm of (Ni/AuGe/Ni) using an electron-beam deposition tool. The Ni acts as a catalyst for the diffusion of Ge dopant into the semiconductor to create a contact with the 2DEG [68]. This diffusion is facilitated by a high-temperature anneal in an inert gas soon after the ohmic contacts are deposited. The bottom of the ohmic recess on the n-side must be below the interface. The ohmic material is then deposited at an angle of 45° to coat the recess sidewalls and make a good contact with the 2DEG. The etched ohmic recess takes advantage of the larger diffusion constant of AuGe in GaAs relative to AlGaAs. The lateral diffusion profile is thus further extended *below* the AlGaAs/GaAs interface, so that the top-gate is not screened by any diffused AuGe in the AlGaAs layer.

p-type contacts use a eutectic mixture of Au and Be. A post-deposition anneal causes the Be dopant to diffuse and contact the 2DHG. For optimum contacts, the ohmic recess must terminate 10-40 nm above the GaAs/AlGaAs interface. Presumably, because the diffusion process is a solid-phase reaction (rather than liquid-phase reaction as in the case of AuGe), the resulting diffusion profile does not screen the top-gate from inducing a 2DHG at the interface.

4.1.3 Top-gate and bond pads

The dimensions of the top-gate define the regions where the 2DEG/2DHG are induced in the mesa. Since the goal is to collect light emitted by the p-n junction, the split top-gate is

fabricated using indium tin oxide (ITO), a *transparent* conductive material. The bond pads do not have this restriction, and are thus fabricated using gold, with an underlying layer of titanium to help adhere to the silicon oxide insulating layer separating these structures from the rest of the device. Four bond pads connect to the two halves of the split top-gate and six additional bond pads connect to the three n-type and three p-type ohmic contacts via holes etched into the insulating oxide layer.

4.2 2DEG/2DHG characterization

The characterization of an undoped 2DEG and 2DHG was carried out using devices having an electron gas or a hole gas (respectively) induced across the entire mesa using a single continuous top-gate (figures 4.3a and 4.3b). All measurements and analyses presented in this section were performed with Dr. Francois Sfigakis from the Coherent Spintronics group. Two additional ohmic contacts are present at the middle of each device

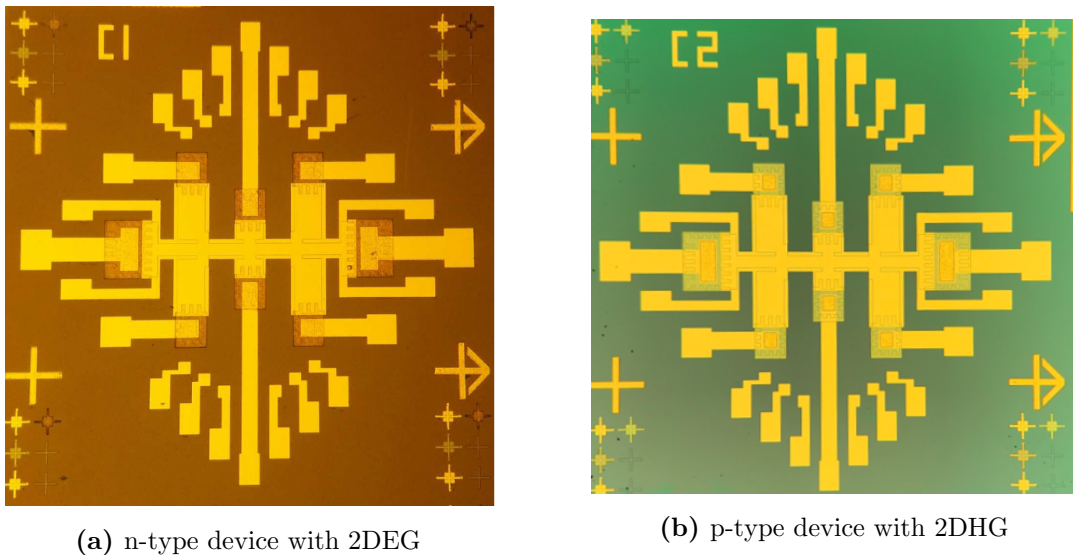


Figure 4.3: n-type and p-type devices fabricated for the characterization of 2DEGs and 2DHGs. *Aside:* The difference in background colour is because the n-type device used Al_2O_3 as the insulating material, while the p-type device used SiO_2 .

for redundancy. The top-gate and bond pads share the same material (Ti/Au), since there is no requirement to extract light from these devices. To separate the 2DEG/2DHG resistances from other contributions to the total resistance of the device (including ohmic contacts, wiring, filters, etc.), a four-terminal measurement setup is used (figure 4.4). Current passes through the 2DEG/2DHG via contacts 4 and 8. The longitudinal voltage V_{xx} is measured across any one of the pairs of contacts (5, 7), (5, 6), (6, 7), (3, 1), (3, 2) or (2, 1). The Hall voltage V_{xy} is measured across any one of (3, 5), (2, 6) or (1, 7).

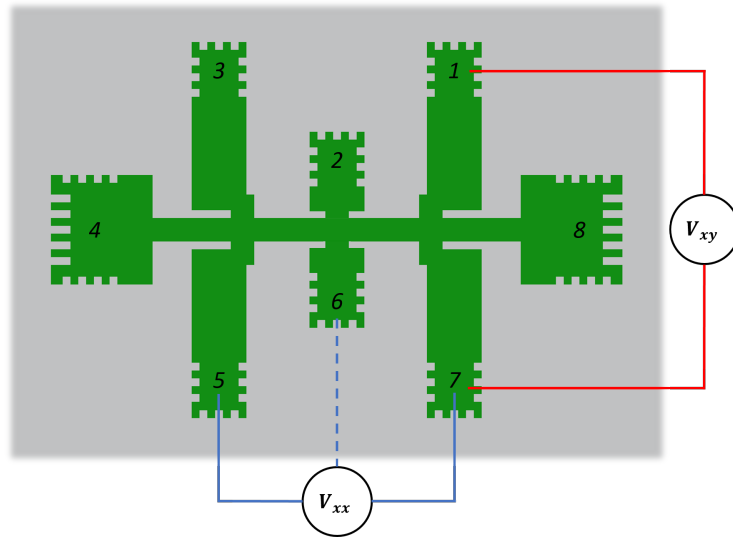


Figure 4.4: Four-terminal measurement setup to determine I-V characteristics, observe magnetoresistance phenomena and extract carrier density and mobility.

4.2.1 Magnetoresistance

Magnetoresistance measurements of the 2DEG and 2DHG follow the theory outlined in section 2.2.1. The device is placed in a 1.4 K helium cryostat equipped with a variable electromagnetic field. The B -field applied perpendicular to the sample is swept from 0 T to 5 T in average steps of 3 mT. The Hall and Shubnikov-de Haas measurements for a 2DEG and 2DHG are shown in figures 4.5 and 4.6 respectively. The integer quantum Hall plateaus and Shubnikov-de Haas oscillations are very clearly defined in the case of the

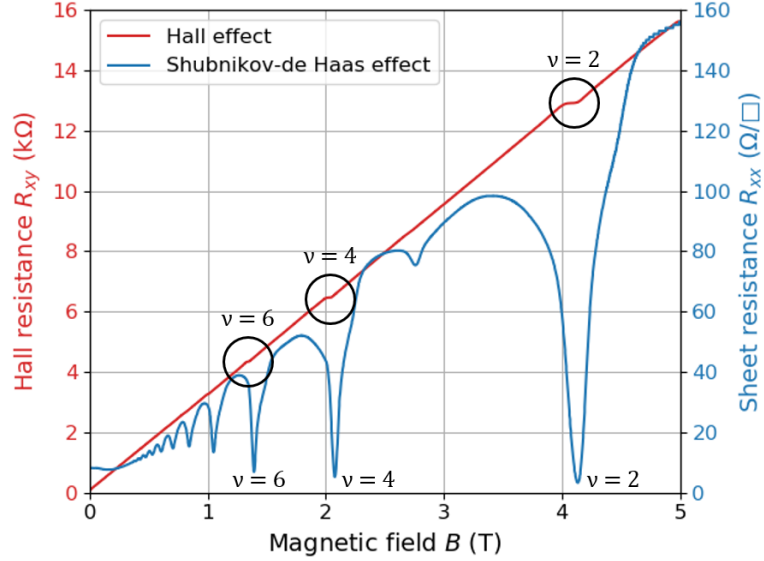


Figure 4.5: Magnetoresistance measurements of an induced 2DEG in an undoped GaAs/AlGaAs heterojunction device. The quantum Hall plateaus (red) and the Shubnikov-de Haas oscillations (blue) are visible.

2DEG. The plateaus at $R_{xy} = 12.906 \text{ k}\Omega$, $6.453 \text{ k}\Omega$ and $4.340 \text{ k}\Omega$ correspond to Landau level fill factors (ν) of 2, 4 and 6 respectively. The B -field values at which the minimas in R_{xx} occur correlate with the B -field at these integer values of ν . This unambiguously proves the existence of a 2DEG in our devices. (*Note:* The absence of the $\nu = 1$ Hall plateau is due to the requirement of a magnetic field larger than 5 T to observe it, which exceeds the capabilities of our cryostat. Shubnikov-de Haas dips and Hall plateaus for the $\nu = 3$ and $\nu = 5$ levels are not visible since they correspond to a Fermi energy at the spin gap rather than the cyclotron gap (figure 2.7), which require also require high magnetic fields to resolve.)

The Hall plateaus and Shubnikov-de Haas oscillations are much less pronounced in the 2DHG sample. Since the effective hole mass in GaAs is about five times the effective electron mass ($m_h^*/m_e^* = 0.34/0.067$), the spacing between successive Landau levels (proportional to $\hbar\omega_c = eB/m_h^*$) is a factor of five smaller in a 2DHG. This makes $\hbar\omega_c$ comparable to the energy broadening δE at each Landau level, and the resulting lack of level separation

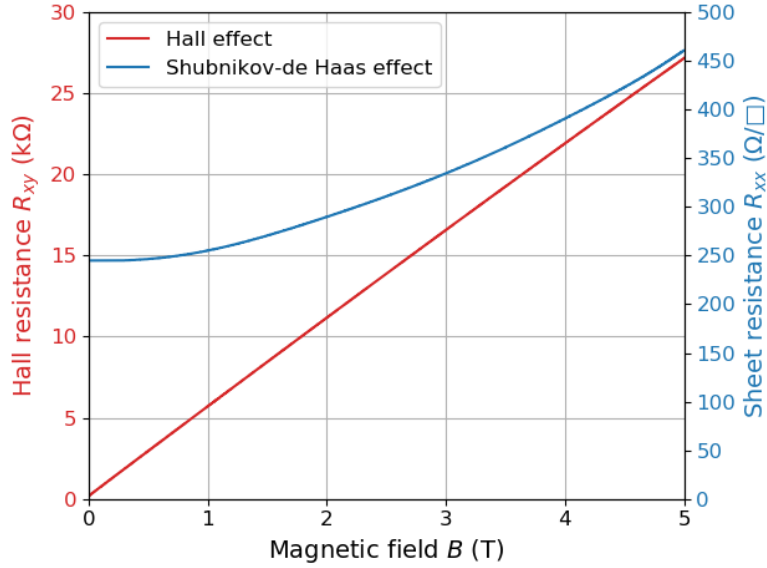
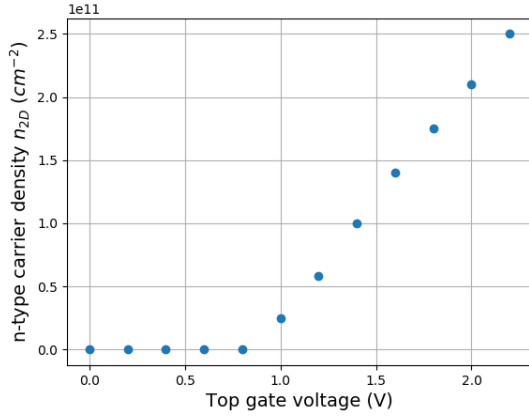


Figure 4.6: Magnetoresistance measurements of an induced 2DHG in an undoped GaAs/AlGaAs heterojunction device.

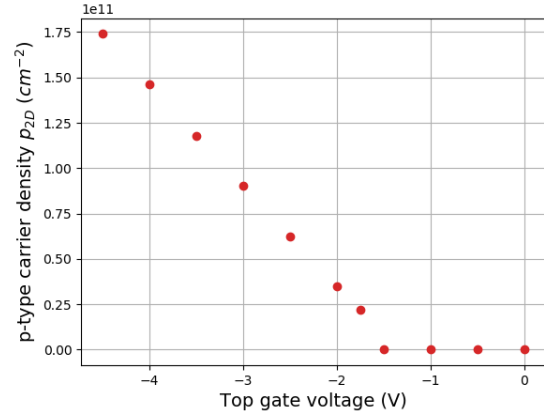
erases the oscillations in R_{xx} and plateaus in R_{xy} . However this does *not* mean that the 2DHG does not exist, it only means their existence cannot be confirmed via the current magnetoresistance measurement setup. By lowering the sample temperature from 1.4 K to 300 mK, the broadening δE will reduce, and make the R_{xx} oscillations and R_{xy} plateaus visible.

4.2.2 Carrier densities and mobilities

The carrier densities and mobilities of the 2DEG and 2DHG were obtained from longitudinal source-drain measurements for different top-gate inducing voltages at zero B -field using equations 2.11 and 2.13. The *turn-on* gate voltage values at which the 2DEG and 2DHG were respectively induced are 1.00 V and -1.75 V (figure 4.7). Above these values, V_{TG} and n_{2D} , p_{2D} share a nearly linear relationship with no hysteresis, indicating that there is no gate leakage and no charge build-up in the layered structure (e.g. in the dielectric). (*Note:* The small non-linearities are most likely due to the use of Al_2O_3 as a



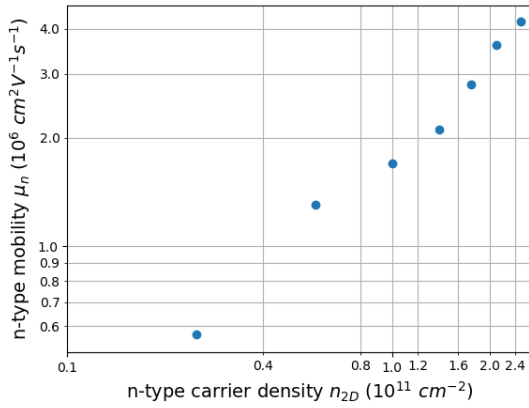
(a) 2DEG



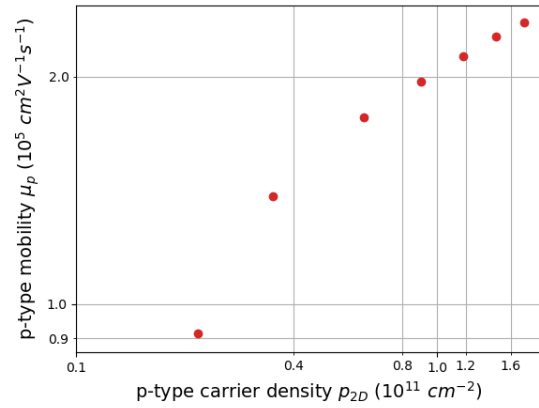
(b) 2DHG

Figure 4.7: Top-gate voltage versus two-dimensional carrier densities for a 2DEG and 2DHG.

dielectric instead of SiO_2). Figure 4.8 shows the n- and p-type carrier mobilities for a range of carrier densities. The p-type mobilities are an order of magnitude lower than the n-type



(a) 2DEG



(b) 2DHG

Figure 4.8: Density-mobility relationship for carriers in a 2DEG and 2DHG.

mobilities.

4.2.3 I-V measurements

Figures 4.9 and 4.10 show the linear ohmic relationship at 4 K between the source-drain bias and resulting current for a device with an induced 2DEG and induced 2DHG respectively. The 2DEG is induced at $V_{TG} = +2.0$ V. The measured resistance of $R_n = 1.03$

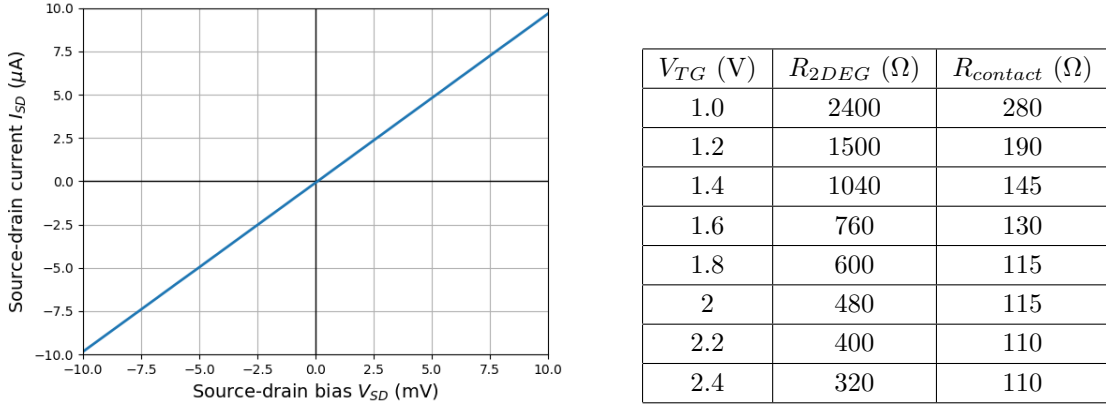


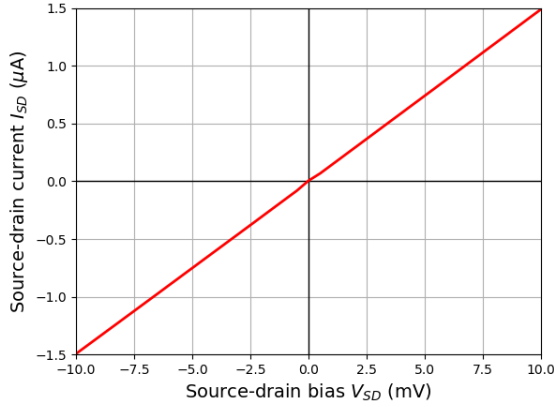
Figure 4.9: Ohmic behaviour of a 2DEG. **Table 4.1:** 2DEG and contact resistances $V_{TG} = +2.0$ V, $R_n = 1.03$ k Ω .

k Ω includes the 2DEG resistance (R_{2DEG}), two ohmic contact resistances ($2R_{contact}$) and additional series resistances (R_{series}) in the measurement setup. Individual values for R_{2DEG} and $R_{contact}$ at different V_{TG} values are shown in table 4.1 and calculated using the equations

$$R_n^{4-8} = R_{2DEG} + 2R_{contact} + R_{series}; \quad (4.1a)$$

$$R_n^{4-6} = 0.5R_{2DEG} + 2R_{contact} + R_{series}. \quad (4.1b)$$

The superscripts 4-8 and 4-6 refer to the location of the contacts used for the two-terminal measurements (refer to figure 4.4). Here, it is assumed that all ohmic contacts possess equal contact resistances. Both R_{2DEG} and $R_{contact}$ decrease with increasing gate voltage. Although $R_{contact}$ saturates around 1.8 V, its value is well under 1 k Ω , which is acceptable for our purposes. The 2DHG in the p-type device is induced at $V_{TG} = -3.25$ V. The I-V relationship is linear and ohmic. As expected, the 2DHG resistances are greater than that



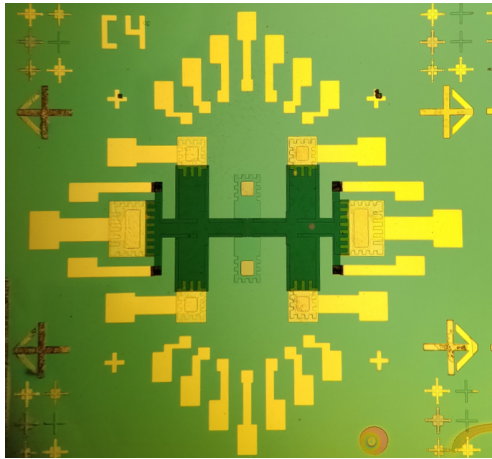
V_{TG} (V)	R_{2DHG} (k Ω)	$R_{contact}$ (k Ω)
-1.6	118.16	44.47
-1.8	39.96	6.81
-2.0	21.24	3.05
-2.2	14.64	1.83
-2.4	11.36	1.17
-2.6	9.16	0.83
-2.8	7.62	0.62
-3.0	6.44	0.50

Figure 4.10: Ohmic behaviour of a 2DHG. **Table 4.2:** 2DHG and contact resistances $V_{TG} = -3.25$ V, $R_p = 6.67$ k Ω .

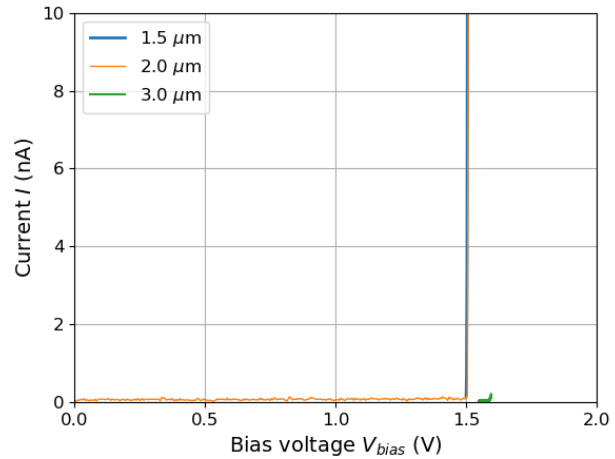
of the 2DEG by about an order of magnitude (table 4.2). Again, both R_{2DHG} and $R_{contact}$ decrease with increasing V_{TG} ; at high carrier densities, the contact resistance is under 1 k Ω .

4.3 Diode behaviour

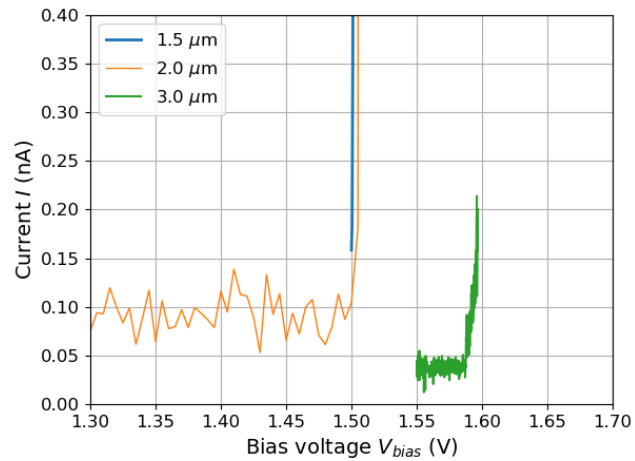
The fabricated p-n junction diode with a 2DEG induced on the left and a 2DHG induced on the right is shown in figure 4.11a. Three separate devices were fabricated, each with a different gap between the two halves of the split ITO top-gate. Measurements and analyses in this section were also conducted with Dr. Sfigakis. Figure 4.11b shows I-V curves for devices with split gaps of 1.5 μm , 2.0 μm and 3.0 μm . All three devices successfully exhibited diode behaviour, with turn-on voltages of approximately 1.5 V. The devices were all unstable to certain extents; the 2.0 μm and 3.0 μm gap devices were worse-off and exhibited an increasing drift in the turn-on bias with time. Figure 4.12 depicts this drift for the 2.0 μm device. The 3 μm device was even more unstable, making it hard to capture data depicting the accurate turn-on voltage of 1.5 V (figure 4.11c). Since the gap between the top-gates results in an insulating region at the level of the single heterojunction, charges are possibly dumped into the substrate at this region as they try to cross the length of the



(a) Fabricated p-n junction



(b) I-V curves



(c) I-V curves (magnified)

Figure 4.11: Picture of fabricated p-n junction diode along with I-V curves for three devices with different top-gate separations.

device. This in turn could create a negative bias that has to be overcome on a subsequent voltage sweep. This is more likely to happen in devices with larger gate separations.

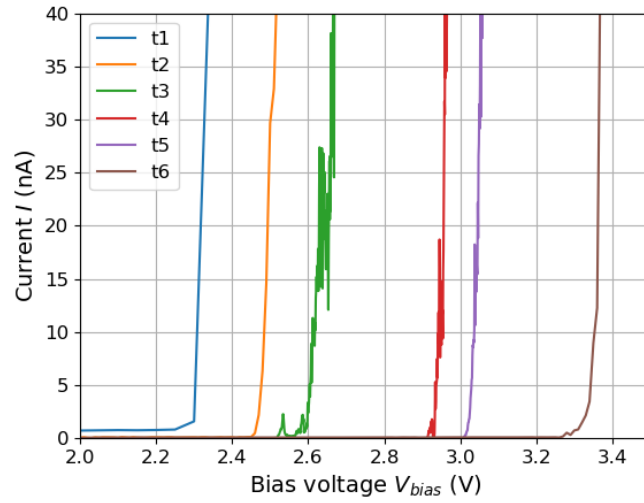


Figure 4.12: Diode behaviour of a p-n junction in an undoped single heterojunction device measured at increasing time intervals t1 through t6. The gate separation is $2.0 \mu\text{m}$.

Chapter 5

Summary & future work

This thesis has aimed to lay the groundwork for the development of the next generation of quantum light emitters using novel semiconductor materials and architectures.

Chapter 2 introduced the theory behind the deterministic generation of single and entangled photons. A specific focus was held on optically-driven semiconductor quantum dots, as well as electrically-driven light emission in quantum wells. Techniques to engineer the environment surrounding the sources to boost extraction efficiency were also covered.

Chapter 3 detailed the results of a finite-difference-time-domain model of a semiconductor nanowire quantum dot source. Optimized architectural parameters that boosted the source transmission efficiency while maintaining a symmetric Gaussian emission profile in the far-field were calculated. Additionally, the Gaussian nature of the far-field emission profile of an existing gated nanowire quantum dot source was calculated to verify that the emissions from such sources are not compromised by the surrounding structures.

Chapter 4 laid out the preliminary results in the development of an all-electric quantum emitter that aims to combine a single-parameter electron pump with a wide two-dimensional p-n junction created by inducing an electron and hole charge carrier gas adjacent to each other in a quantum well device. A p-n junction diode was successfully fabricated in a single heterojunction device and characterized.

These results pave the road towards the creation of bright sources of photons with high

entanglement fidelities and modal properties. The following sections propose the potential next steps to follow to reach this goal.

5.1 Gated nanowire source optimized for brightness

With the optimized nanowire source parameters obtained in chapter 3, a bright, deterministic source of single and entangled photons can be fabricated by integrating metallic gates around the source to effectively erase any finestructure splitting that is present in the quantum dot. A suitable technique must be developed to electrically isolate the gates from the semiconductor substrate *without* having to coat the entire nanowire in dielectric material, since this compromises the source brightness and to some extent the tightness of the outgoing beam.

5.2 Integrating an electron pump and a narrow p-n junction

The p-n junction device described in chapter 4 is a proof-of-concept prototype towards the creation of an electrically driven quantum emitter. Subsequent devices must be fabricated using a GaAs/AlGaAs quantum well substrate, such as the one in figure 5.1. The GaAs quantum well offers tighter carrier confinement than a single heterojunction, and helps keep carriers confined as they cross the insulation barrier between the p- and n-side of the device. Additionally, the junctions must be narrowed to prevent electrons from being dumped in large numbers at once onto the p-side. This will also help in the subsequent integration of Schottky gates for an electron pump. Additional gates on the p-side can create quantization of heavy holes, which can control the spin properties of the recombining electron-hole pairs, and thus create quantum correlations between emitted photons.

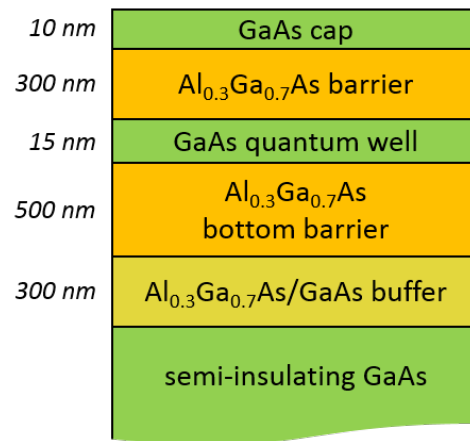


Figure 5.1: GaAs/AlGaAs heterostructure with a quantum well.

Letter of copyright permission

Below is a copy of the license document from American Institute of Physics (AIP) Publishing granting permission to use the data plot in figure 2.6.

AIP PUBLISHING LICENSE TERMS AND CONDITIONS

Jan 23, 2019

This Agreement between Nachiket S Sherlekar ("You") and AIP Publishing ("AIP Publishing") consists of your license details and the terms and conditions provided by AIP Publishing and Copyright Clearance Center.

License Number	4514420017661
License date	Jan 22, 2019
Licensed Content Publisher	AIP Publishing
Licensed Content Publication	Applied Physics Letters
Licensed Content Title	Fabrication of high-quality one- and two-dimensional electron gases in undoped GaAs/AlGaAs heterostructures
Licensed Content Author	R. H. Harrell, K. S. Pyshkin, M. Y. Simmons, et al
Licensed Content Date	Apr 19, 1999
Licensed Content Volume	74
Licensed Content Issue	16
Type of Use	Thesis/Dissertation
Requestor type	Student
Format	Print and electronic
Portion	Figure/Table
Number of figures/tables	1
Title of your thesis / dissertation	Next-Generation Solid-State Quantum Emitters

Expected completion date	Jan 2019
Estimated size (number of pages)	86
Requestor Location	Mr. Nachiket Sherlekar [personal address redacted]
Billing Type	Waterloo, ON Canada Attn: Mr. Nachiket Sherlekar Invoice
Billing Address	Mr. Nachiket Sherlekar [personal address redacted]
Total	Waterloo, ON Canada Attn: Mr. Nachiket Sherlekar 0.00 USD

[Terms and Conditions](#)

AIP Publishing -- Terms and Conditions: Permissions Uses

AIP Publishing hereby grants to you the non-exclusive right and license to use and/or distribute the Material according to the use specified in your order, on a one-time basis, for the specified term, with a maximum distribution equal to the number that you have ordered. Any links or other content accompanying the Material are not the subject of this license.

Bibliography

- [1] J. P. Dowling and G. J. Milburn, “Quantum technology: the second quantum revolution,” *Philosophical Transactions of the Royal Society A: Mathematical, Physical and Engineering Sciences*, vol. 361, pp. 1655--1674, Aug. 2003.
- [2] M. Planck, “Ueber das Gesetz der Energieverteilung im Normalspectrum,” *Annalen der Physik*, vol. 309, no. 3, pp. 553--563, 1901.
- [3] G. Kirchhoff, “I. *On the relation between the radiating and absorbing powers of different bodies for light and heat,*” *The London, Edinburgh, and Dublin Philosophical Magazine and Journal of Science*, vol. 20, pp. 1--21, July 1860.
- [4] A. Einstein, “ber einen die Erzeugung und Verwandlung des Lichtes betreffenden heuristischen Gesichtspunkt,” *Annalen der Physik*, vol. 322, no. 6, pp. 132--148, 1905.
- [5] G. G. Claude Cohen-Tannoudji, Jacques Dupont-Roc, *Photons and Atoms: Introduction to Quantum Electrodynamics*. Wiley, 1997.
- [6] A. Einstein, B. Podolsky, and N. Rosen, “Can Quantum-Mechanical Description of Physical Reality Be Considered Complete?,” *Physical Review*, vol. 47, pp. 777--780, May 1935.
- [7] J. S. Bell, “On the Einstein Podolsky Rosen paradox,” *Physics*, vol. 1, pp. 195--200, Nov. 1964.

- [8] A. Aspect, P. Grangier, and G. Roger, “Experimental Realization of Einstein-Podolsky-Rosen-Bohm *Gedankenexperiment* : A New Violation of Bell’s Inequalities,” *Physical Review Letters*, vol. 49, pp. 91--94, July 1982.
- [9] C. H. Bennett and G. Brassard, “Quantum cryptography: Public key distribution and coin tossing,” *Theoretical Computer Science*, vol. 560, pp. 7--11, Dec. 2014.
- [10] A. K. Ekert, “Quantum cryptography based on Bells theorem,” *Physical Review Letters*, vol. 67, pp. 661--663, Aug. 1991.
- [11] L. A. Lugiato, A. Gatti, and E. Brambilla, “Quantum imaging,” *Journal of Optics B: Quantum and Semiclassical Optics*, vol. 4, p. 9, Mar. 2002.
- [12] S. Lloyd, “Enhanced Sensitivity of Photodetection via Quantum Illumination,” *Science*, vol. 321, pp. 1463--1465, Sept. 2008.
- [13] E. Knill, R. Laflamme, and G. J. Milburn, “A scheme for efficient quantum computation with linear optics,” *Nature*, vol. 409, p. 7, Jan. 2001.
- [14] H. J. Kimble, “The quantum internet,” *Nature*, vol. 453, pp. 1023--1030, June 2008.
- [15] M. D. Eisaman, J. Fan, A. Migdall, and S. V. Polyakov, “Invited Review Article: Single-photon sources and detectors,” *Review of Scientific Instruments*, vol. 82, p. 071101, July 2011.
- [16] P. Senellart, G. Solomon, and A. White, “High-performance semiconductor quantum-dot single-photon sources,” *Nature Nanotechnology*, vol. 12, pp. 1026--1039, Nov. 2017.
- [17] D. Huber, M. Reindl, J. Aberl, A. Rastelli, and R. Trotta, “Semiconductor quantum dots as an ideal source of polarization-entangled photon pairs on-demand: a review,” *Journal of Optics*, vol. 20, p. 073002, July 2018.
- [18] I. Aharonovich, D. Englund, and M. Toth, “Solid-state single-photon emitters,” *Nature Photonics*, vol. 10, pp. 631--641, Oct. 2016.

- [19] X.-L. Wang, L.-K. Chen, W. Li, H.-L. Huang, C. Liu, C. Chen, Y.-H. Luo, Z.-E. Su, D. Wu, Z.-D. Li, H. Lu, Y. Hu, X. Jiang, C.-Z. Peng, L. Li, N.-L. Liu, Y.-A. Chen, C.-Y. Lu, and J.-W. Pan, “Experimental Ten-Photon Entanglement,” *Physical Review Letters*, vol. 117, Nov. 2016.
- [20] H. J. Kimble, M. Dagenais, and L. Mandel, “Photon Antibunching in Resonance Fluorescence,” *Physical Review Letters*, vol. 39, pp. 691–695, Sept. 1977.
- [21] F. Diedrich and H. Walther, “Nonclassical radiation of a single stored ion,” *Physical Review Letters*, vol. 58, pp. 203–206, Jan. 1987.
- [22] C. W. Chou, S. V. Polyakov, A. Kuzmich, and H. J. Kimble, “Single-Photon Generation from Stored Excitation in an Atomic Ensemble,” *Physical Review Letters*, vol. 92, p. 213601, May 2004.
- [23] A. Faraon, P. E. Barclay, C. Santori, K.-M. C. Fu, and R. G. Beausoleil, “Resonant enhancement of the zero-phonon emission from a colour centre in a diamond cavity,” *Nature Photonics*, vol. 5, pp. 301–305, May 2011.
- [24] J. Kim, O. Benson, H. Kan, and Y. Yamamoto, “A single-photon turnstile device,” *Nature*, vol. 397, pp. 500–503, Feb. 1999.
- [25] D. Huber, M. Reindl, S. F. C. da Silva, C. Schimpf, J. Martin-Sanchez, H. Huang, G. Piredda, J. Edlinger, A. Rastelli, and R. Trotta, “Strain-tunable GaAs quantum dot: An on-demand source of nearly-maximally entangled photon pairs,” *Physical Review Letters*, vol. 121, July 2018. arXiv: 1801.06655.
- [26] Y. Chen, M. Zopf, R. Keil, F. Ding, and O. G. Schmidt, “Highly-efficient extraction of entangled photons from quantum dots using a broadband optical antenna,” *Nature Communications*, vol. 9, Dec. 2018.
- [27] J. Claudon, J. Bleuse, N. S. Malik, M. Bazin, P. Jaffrennou, N. Gregersen, C. Sauvan, P. Lalanne, and J.-M. Gerard, “A highly efficient single-photon source based on a quantum dot in a photonic nanowire,” *Nature Photonics*, Jan. 2010.

- [28] M. E. Reimer, G. Bulgarini, N. Akopian, M. Hocevar, M. B. Bavinck, M. A. Verheijen, E. P. Bakkers, L. P. Kouwenhoven, and V. Zwiller, “Bright single-photon sources in bottom-up tailored nanowires,” *Nature Communications*, vol. 3, Jan. 2012.
- [29] C. Gies, J. Wiersig, and F. Jahnke, *Quantum Statistical Properties of the Light Emission from Quantum Dots in Microcavities*, p. 1. 2009.
- [30] O. Benson, C. Santori, M. Pelton, and Y. Yamamoto, “Regulated and Entangled Photons from a Single Quantum Dot,” *Physical Review Letters*, vol. 84, pp. 2513--2516, Mar. 2000.
- [31] R. Seguin, A. Schliwa, S. Rodt, K. Ptschke, U. W. Pohl, and D. Bimberg, “Size-Dependent Fine-Structure Splitting in Self-Organized InAs / GaAs Quantum Dots,” *Physical Review Letters*, vol. 95, Dec. 2005.
- [32] G. Bester, S. Nair, and A. Zunger, “Pseudopotential calculation of the excitonic fine structure of million-atom self-assembled In_{1-x}Ga_xAs / GaAs quantum dots,” *Physical Review B*, vol. 67, Apr. 2003.
- [33] M. Bayer, G. Ortner, O. Stern, A. Kuther, A. A. Gorbunov, A. Forchel, P. Hawrylak, S. Fafard, K. Hinzer, T. L. Reinecke, S. N. Walck, J. P. Reithmaier, F. Klopff, and F. Schfer, “Fine structure of neutral and charged excitons in self-assembled In(Ga)As/(Al)GaAs quantum dots,” *Physical Review B*, vol. 65, May 2002.
- [34] R. Singh and G. Bester, “Nanowire Quantum Dots as an Ideal Source of Entangled Photon Pairs,” *Physical Review Letters*, vol. 103, Aug. 2009.
- [35] S. Seidl, M. Kroner, A. Hgele, K. Karrai, R. J. Warburton, A. Badolato, and P. M. Petroff, “Effect of uniaxial stress on excitons in a self-assembled quantum dot,” *Applied Physics Letters*, vol. 88, p. 203113, May 2006.
- [36] E. Poem, Y. Kodriano, C. Tradonsky, N. H. Lindner, B. D. Gerardot, P. M. Petroff, and D. Gershoni, “Accessing the dark exciton with light,” *Nature Physics*, vol. 6, pp. 993--997, Dec. 2010.

- [37] A. Fognini, A. Ahmadi, M. Zeeshan, J. T. Fokkens, S. J. Gibson, N. Sherlekar, S. J. Daley, D. Dalacu, P. J. Poole, K. D. Jns, V. Zwiller, and M. E. Reimer, “Path to perfect photon entanglement with a quantum dot,” *arXiv:1710.10815 [cond-mat, physics:physics, physics:quant-ph]*, Oct. 2017. arXiv: 1710.10815.
- [38] T. Kuroda, T. Mano, N. Ha, H. Nakajima, H. Kumano, B. Urbaszek, M. Jo, M. Abbarchi, Y. Sakuma, K. Sakoda, I. Suemune, X. Marie, and T. Amand, “Symmetric quantum dots as efficient sources of highly entangled photons: Violation of Bell’s inequality without spectral and temporal filtering,” *Physical Review B*, vol. 88, July 2013.
- [39] Y. H. Huo, A. Rastelli, and O. G. Schmidt, “Ultra-small excitonic fine structure splitting in highly symmetric quantum dots on GaAs (001) substrate,” *Applied Physics Letters*, vol. 102, p. 152105, Apr. 2013.
- [40] J. Skiba-Szymanska, R. M. Stevenson, C. Varnava, M. Felle, J. Huwer, T. Mller, A. J. Bennett, J. P. Lee, I. Farrer, A. B. Krysa, P. Spencer, L. E. Goff, D. A. Ritchie, J. Heffernan, and A. J. Shields, “Universal Growth Scheme for Quantum Dots with Low Fine-Structure Splitting at Various Emission Wavelengths,” *Physical Review Applied*, vol. 8, July 2017.
- [41] A. J. Bennett, M. A. Pooley, R. M. Stevenson, M. B. Ward, R. B. Patel, A. B. de la Giroday, N. Skld, I. Farrer, C. A. Nicoll, D. A. Ritchie, and A. J. Shields, “Electric-field-induced coherent coupling of the exciton states in a single quantum dot,” *Nature Physics*, vol. 6, pp. 947--950, Dec. 2010.
- [42] R. M. Stevenson, R. J. Young, P. Atkinson, K. Cooper, D. A. Ritchie, and A. J. Shields, “A semiconductor source of triggered entangled photon pairs,” *Nature*, vol. 439, pp. 179-182, Jan. 2006.
- [43] J. Wang, M. Gong, G.-C. Guo, and L. He, “Eliminating the fine structure splitting of excitons in self-assembled InAs/GaAs quantum dots via combined stresses,” *Applied Physics Letters*, vol. 101, p. 063114, Aug. 2012.

- [44] P. E. Kremer, A. C. Dada, P. Kumar, Y. Ma, S. Kumar, E. Clarke, and B. D. Gerardot, “Strain-tunable quantum dot embedded in a nanowire antenna,” *Physical Review B*, vol. 90, Nov. 2014.
- [45] A. Fognini, A. Ahmadi, S. J. Daley, M. E. Reimer, and V. Zwiller, “Universal fine-structure eraser for quantum dots,” *Optics Express*, vol. 26, p. 24487, Sept. 2018.
- [46] M. Zeeshan, N. Sherlekar, A. Ahmadi, R. L. Williams, and M. E. Reimer, “Quadrupole electric field for erasing the fine structure splitting in a single quantum dot,” p. 8, sep 2018.
- [47] T. Ando, A. B. Fowler, and F. Stern, “Electronic properties of two-dimensional systems,” *Reviews of Modern Physics*, vol. 54, pp. 437--672, Apr. 1982.
- [48] H. L. Strmer, R. Dingle, A. C. Gossard, W. Wiegmann, and M. D. Sturge, “Two-dimensional electron gas at a semiconductor-semiconductor interface,” *Solid State Communications*, vol. 29, no. 10, pp. 705 -- 709, 1979.
- [49] R. H. Harrell, K. S. Pyshkin, M. Y. Simmons, D. A. Ritchie, C. J. B. Ford, G. A. C. Jones, and M. Pepper, “Fabrication of high-quality one- and two-dimensional electron gases in undoped GaAs/AlGaAs heterostructures,” *Applied Physics Letters*, vol. 74, pp. 2328--2330, Apr. 1999.
- [50] K. v. Klitzing, G. Dorda, and M. Pepper, “New Method for High-Accuracy Determination of the Fine-Structure Constant Based on Quantized Hall Resistance,” *Physical Review Letters*, vol. 45, pp. 494--497, Aug. 1980.
- [51] K. Flensberg, A. A. Odintsov, F. Liefrink, and P. Teunissen, “Towards single-electron metrology,” *International Journal of Modern Physics B*, vol. 13, pp. 2651--2687, Sept. 1999. arXiv: cond-mat/9908219.
- [52] M. W. Keller, N. M. Zimmerman, and A. L. Eichenberger, “Uncertainty budget for the NIST electron counting capacitance standard, ECCS-1,” *Metrologia*, vol. 44, pp. 505--512, Dec. 2007.

- [53] B. Kaestner and V. Kashcheyevs, “Non-adiabatic quantized charge pumping with tunable-barrier quantum dots: a review of current progress,” *Reports on Progress in Physics*, vol. 78, p. 103901, Oct. 2015.
- [54] S. P. Giblin, M. Kataoka, J. D. Fletcher, P. See, T. J. B. M. Janssen, J. P. Griffiths, G. A. C. Jones, I. Farrer, and D. A. Ritchie, “Towards a quantum representation of the ampere using single electron pumps,” *Nature Communications*, vol. 3, Jan. 2012. arXiv: 1201.2533.
- [55] M. Seo, Y.-H. Ahn, Y. Oh, Y. Chung, S. Ryu, H.-S. Sim, I.-H. Lee, M.-H. Bae, and N. Kim, “Improvement of electron pump accuracy by a potential-shape-tunable quantum dot pump,” *Physical Review B*, vol. 90, Aug. 2014.
- [56] O. Gazzano, S. Michaelis de Vasconcellos, C. Arnold, A. Nowak, E. Galopin, I. Sagnes, L. Lanco, A. Lematre, and P. Senellart, “Bright solid-state sources of indistinguishable single photons,” *Nature Communications*, vol. 4, Dec. 2013.
- [57] G. Bulgarini, M. E. Reimer, M. Bouwes Bavinck, K. D. Jns, D. Dalacu, P. J. Poole, E. P. A. M. Bakkers, and V. Zwiller, “Nanowire Waveguides Launching Single Photons in a Gaussian Mode for Ideal Fiber Coupling,” *Nano Letters*, vol. 14, pp. 4102--4106, July 2014.
- [58] H. Wang, Y. He, Y.-H. Li, Z.-E. Su, B. Li, H.-L. Huang, X. Ding, M.-C. Chen, C. Liu, J. Qin, J.-P. Li, Y.-M. He, C. Schneider, M. Kamp, C.-Z. Peng, S. Hfiling, C.-Y. Lu, and J.-W. Pan, “High-efficiency multiphoton boson sampling,” *Nature Photonics*, vol. 11, pp. 361--365, May 2017.
- [59] L. Tong, J. Lou, and E. Mazur, “Single-mode guiding properties of subwavelength-diameter silica and silicon wire waveguides,” *Optics Express*, vol. 12, no. 6, p. 1025, 2004.
- [60] E. M. Purcell, “Spontaneous emission probabilities at radio frequencies,” *Physical Review*, vol. 69, p. 681, Jun 1946.

- [61] I. Friedler, C. Sauvan, J. P. Hugonin, P. Lalanne, J. Claudon, and J. M. Grard, “Solid-state single photon sources: the nanowire antenna,” *Optics Express*, vol. 17, p. 2095, Feb. 2009.
- [62] J. Claudon, N. Gregersen, P. Lalanne, and J.-M. Grard, “Harnessing Light with Photonic Nanowires: Fundamentals and Applications to Quantum Optics,” *ChemPhysChem*, vol. 14, pp. 2393--2402, Aug. 2013.
- [63] J. Grard, B. Sermage, B. Gayral, B. Legrand, E. Costard, and V. Thierry-Mieg, “Enhanced Spontaneous Emission by Quantum Boxes in a Monolithic Optical Microcavity,” *Physical Review Letters*, vol. 81, pp. 1110--1113, Aug. 1998.
- [64] J. Bleuse, J. Claudon, M. Creasey, N. S. Malik, J.-M. Grard, I. Maksymov, J.-P. Hugonin, and P. Lalanne, “Inhibition, Enhancement, and Control of Spontaneous Emission in Photonic Nanowires,” *Physical Review Letters*, vol. 106, Mar. 2011.
- [65] P. Caroff, J. Bolinsson, and J. Johansson, “Crystal phases in iii--v nanowires: From random toward engineered polytypism,” *IEEE Journal of Selected Topics in Quantum Electronics*, vol. 17, pp. 829--846, July 2011.
- [66] D. Dalacu, K. Mnaymneh, J. Lapointe, X. Wu, P. J. Poole, G. Bulgarini, V. Zwiller, and M. E. Reimer, “Ultraclean Emission from InAsP Quantum Dots in Defect-Free Wurtzite InP Nanowires,” *Nano Letters*, vol. 12, pp. 5919--5923, Nov. 2012.
- [67] D. Dalacu, K. Mnaymneh, X. Wu, J. Lapointe, G. C. Aers, P. J. Poole, and R. L. Williams, “Selective-area vapor-liquid-solid growth of tunable InAsP quantum dots in nanowires,” *Applied Physics Letters*, vol. 98, p. 251101, June 2011.
- [68] M. Powers, J. Staroba, and C.-C. Cheng, “The Effect of Ni Content on Lateral Diffusion of Alloyed Au-Ni-AuGe Ohmic Contacts in GaAs-AlGaAs-InGaAs pHEMT Structures,” p. 4, 2014.

Appendix A

Lumerical FDTD script files

A.1 Infinitely long cylindrical nanowire

```
1 #Extracts the Purcell factor, transmission and effective refractive index of an infinitely long
   InP nanowire sweeping over diameter
2 deleteall;
3 #Initializing input variables
4 d = 0.2e-6;      #Default diameter (m)
5 n = 3.4;        #Refractive Index of InP
6 lambda = 890e-9; #Source wavelength
7 #Simulation region
8 addfdtd;
9 set("x", 0); set("y", 0); set("z", 0);
10 set("x_span", 5e-6);
11 set("y_span", 5e-6);
12 set("z_span", 10e-6);
13 #Nanowire geometry
14 addcircle; set("name", "NW");
15 set("x", 0); set("y", 0); set("z", 0);
16 set("radius", d/2); set("z_span", 12e-6);
17 set("material", "<Object_defined_dielectric>");
18 set("index", n);
19 dia = 80e-9:5e-9:400e-9; #Diameter sweep vector (m)
20 l = length(dia);
21 #Preallocating for output variables
22 purcell_fac = matrix(l);
23 transm = matrix(l);
24 n_eff = matrix(l);
25 #Monitor to extract effective refractive index (neff)
```

```

26 addmodeexpansion; set("name", "mode_exp");
27 set("monitor_type", "2D_Z-normal");
28 set("x", 0); set("y", 0); set("z", 0);
29 set("x_span", 2e-6); set("y_span", 2e-6);
30 set("mode_selection", "fundamental_mode");
31 set("override_global_monitor_settings", 1);
32 set("wavelength_center", lambda);
33 set("wavelength_span", 0);
34 #Monitor to extract transmission
35 addpower; set("name", "Transmission");
36 set("monitor_type", "2D_Z-normal");
37 set("x", 0); set("y", 0); set("z", 4.9e-6);
38 #Quantum dot
39 adddipole; set("name", "QD");
40 set("x", 0); set("y", 0); set("z", 0);
41 set("theta", 90);
42 set("center_wavelength", 890e-9);
43 set("wavelength_span", 0);
44 #Loop to extract Purcell factor, transmission and neff for different diameters
45 for(i = 1:1)
46 {
47     switchtolayout;
48     select("NW");
49     set("radius", dia(i)/2);
50     select("Transmission");
51     set("x_span", 1.5*dia(i));
52     set("y_span", 1.5*dia(i));
53     ?"Running_simulation_"+num2str(i)+"_of_"+num2str(1);
54     run;
55     purc = getresult("QD", "purcell");
56     purcell_fac(i) = purc.purcell;
57     tran = getresult("Transmission", "T");
58     transm(i) = tran.T;
59     effri = getresult("mode_exp", "neff");
60     n_eff(i) = real(effri.neff);
61 }
62 #Writing data to text files
63 write("Fp_" + num2str(dia(1))+"nm_"+num2str(dia(1))+"nm.txt", num2str(purcell_fac));
64 write("Effective_RI_" + num2str(dia(1))+"nm_"+num2str(dia(1))+"nm.txt", num2str(n_eff));
65 write("Transmission_infwire_" + num2str(dia(1))+"nm_"+num2str(dia(1))+"nm.txt", num2str(transm));

```

A.2 Diameter and dot height sweep to maximize transmission

```

1 #Script to sweep over NW diameter QD z-position and obtain Purcell factors and Transmission

```

```

    values for a tapered NW.
2 deleteall;
3 d = 0.23e-6;      #Default diameter
4 ht = 1.5e-6;     #Cylindrical base height
5 n = 3.4;         #Refractive index of InP
6 lambda = 890e-9; #Emitter wavelength
7 #Simulation region:
8 addfdtd;
9 set("x", 0); set("y", 0); set("z", 0);
10 set("x_span", 10e-6); set("y_span", 10e-6); set("z_min", -6.5e-6);
11 set("z_max", 4.5e-6); set("z_min_bc", "Metal");
12 #Nanowire:
13 addstructuregroup;
14 set("name", "NW");
15 set("x", 0); set("y", 0); set("z", 0);
16 adduserprop("material", 5, "<Object_defined_dielectric>");
17 adduserprop("index", 0, n); adduserprop("theta", 0, 2);
18 adduserprop("radius", 2, d/2); adduserprop("ht_base", 2, ht);
19 set("construction_group", 1);
20 set("script", read("Cone_Mirrored_Setup_Script.txt"));
21 #Sweep vectors
22 qdht = 0.2e-6:0.05e-6:1.4e-6; lqd = length(qdht);
23 dia = 205e-9:1e-9:249e-9;      ld = length(dia);
24 #Initializing
25 purcell_fac = matrix(lqd, ld);
26 transm = matrix(lqd, ld);
27 ht_cone = matrix(ld);
28 #Power monitor to extract transmission
29 addpower; set("name", "Transmission");
30 set("x", 0); set("y", 0);
31 set("x_span", 10e-6); set("y_span", 10e-6);
32 #Dipole to model quantum dot
33 adddipole; set("name", "QD");
34 set("x", 0); set("y", 0); set("theta", 90);
35 set("center_wavelength", 890e-9);
36 set("wavelength_span", 0); set("optimize_for_short_pulse", 0);
37 counter = 0;
38 for(j = 1:lqd)
39     {
40     for(k = 1:ld)
41         {
42         switchtolayout; select("NW"); set("radius", dia(k)/2);
43         ht_cone(k) = (dia(k)/2)/tan(2*pi/360);
44         select("FDTD"); set("z_min", -(ht + ht_cone(k)/2));
45         select("QD"); set("x", 0); set("y", 0); set("z", -(ht + ht_cone(k)/2) + qdht(j));
46         select("Transmission"); set("z", ht_cone(k)/2);
47         counter = counter + 1;
48         ?"Running_simulation_" + num2str(counter) + "_of_" + num2str(ld*lqd);

```

```

49     run;
50     purc = getresult("QD", "purcell"); purcell_fac(j, k) = purc.purcell;
51     trans = getresult("Transmission", "T"); transm(j, k) = trans.T;
52     }
53 }
54 #Matrix indices corresponding to max transmission
55 Tmax = max(transm); Tmax_index = find(transm == Tmax);
56 jmax = mod(Tmax_index, lqd); kmax = (Tmax_index - jmax)/lqd + 1;
57 #Writing max transmission and corresponding NW diameter, QD z-position and Purcell factor to
    file
58 write("Max_transmission2.txt", "T_=" + num2str(Tmax));
59 write("Max_transmission2.txt", "Fp_=" + num2str(purcell_fac(jmax, kmax)));
60 write("Max_transmission2.txt", "Normalized_T_=" + num2str(Tmax/purcell_fac(jmax, kmax)));
61 write("Max_transmission2.txt", "QD_z-position_=" + num2str(qdht(jmax)));
62 write("Max_transmission2.txt", "Diameter_=" + num2str(dia(kmax)));
63 #Writing all Purcell factor and transmission values into matrices
64 write("Fp_QDz.txt", num2str(purcell_fac));
65 write("Transmission_QDz.txt", num2str(transm));

```

A.2.1 Setup script

```

1 #Cone_Mirrored_Setup_Script.txt
2 #Equation for conical taper
3 z_span = radius/tan(theta*pi/360);
4 eqn = num2str(radius/z_span)+"*(x"+num2str(z_span*(0.5)*1e6)+")";
5 #Conical taper
6 addcustom; set("name", "cone");
7 set("x", 0); set("y", 0); set("z", 0);
8 set("create_3D_object_by", "revolution");
9 set("x_span", z_span); set("y_span", 2*radius); set("z_span", 2*radius);
10 set("equation_1", eqn); set("first_axis", "y"); set("rotation_1", 90);
11 set("material", material);
12 if(get("material")=="<Object_defined_dielectric>")
13 { set("index", index); }
14 #Cylindrical base
15 addcircle; set("name", "base");
16 set("x", 0); set("y", 0); set("z", -(z_span + ht_base)/2);
17 set("radius", radius); set("z_span", ht_base); set("material", material);
18 if(get("material")=="<Object_defined_dielectric>")
19 { set("index", index); }

```

A.3 Gated InP nanowire with Al₂O₃ dielectric cladding

```

1 #Extract transmission efficiency and far-field emission profile of gated NW structure with
    rounded tip dielectric cladding

```

```

2 deleteall;
3 d = 0.220e-6;      #NW Diameter (m)
4 clad_t = 0.15e-6; #Clad thickness (m)
5 n_NW = 3.4;       #NW RI (AlGaAs)
6 n_clad = 1.76;    #Clad RI (Al2O3)
7 n_sub = 3.66;     #substrate RI (GaAs)
8 r_tip = 0.05e-6;  #Clad round tip radius (m)
9 #Simulation region:
10 addfdtd;
11 set("x", 0); set("y", 0); set("z", 0);
12 set("x_span", 7e-6);
13 set("y_span", 7e-6);
14 set("z_min", -5e-6);
15 set("z_max", 7.5e-6);
16 #Entire structure:
17 addstructuregroup;
18 set("name", "Gated_roundtip_NW");
19 set("x", 0); set("y", 0); set("z", 0);
20 #AlGaAs Nanowire:
21 adduserprop("NW_mat", 5, "<Object_defined_dielectric>");
22 adduserprop("NW_RI", 0, n_NW);
23 adduserprop("alpha1", 0, 2); #Tapering angle (full angle) in degrees
24 adduserprop("radius", 2, d/2);
25 adduserprop("ht_base", 2, 1e-6); #Height of cylindrical base
26 #Al2O3 dielectric cladding:
27 adduserprop("clad_mat", 5, "<Object_defined_dielectric>");
28 adduserprop("clad_RI", 0, n_clad);
29 adduserprop("clad_t", 2, clad_t);
30 adduserprop("r_tip", 2, r_tip);
31 adduserprop("alpha2", 0, 4.62); #Cladding tapering angle (full angle)
32 #Substrate:
33 adduserprop("sub_mat", 5, "<Object_defined_dielectric>");
34 adduserprop("sub_RI", 0, n_sub);
35 adduserprop("sx", 2, 12e-6);
36 adduserprop("sy", 2, 12e-6);
37 adduserprop("sz", 2, 5e-6);
38 #Au gates:
39 adduserprop("gate_mat", 5, "Au_(Gold)_Palik");
40 adduserprop("gl", 2, 1e-6);
41 adduserprop("gw", 2, 0.1e-6);
42 adduserprop("gh", 2, 0.1e-6);
43 set("construction_group", 1);
44 set("script", read("Gated_roundtip_Setup.txt"));
45 runsetup;
46 #Extracting z-coordinates for the placement of QD dipole and power monitor
47 select("Gated_roundtip_NW:Gate1");
48 z_QD = get("z");
49 select("Gated_roundtip_NW:clad_tip");

```

```

50 z_p1 = get("x_span");
51 z_p2 = get("z");
52 z_power = z_p1/2 + z_p2;
53 addanalysisgroup;
54 set("name", "Gated_roundtip_analysis");
55 set("x", 0); set("y", 0); set("z", 0);
56 adduserprop("QD_center_wavelength", 2, 890e-9);
57 adduserprop("QD_wavelength_span", 2, 0);
58 adduserprop("z_QD", 2, z_QD);
59 adduserprop("z_power", 2, z_power);
60 set("setup_script", read("Gated_NW_Analysis_Script.txt"));
61 run;

```

A.3.1 Setup script

```

1 #Gated_roundtip_Setup.txt
2 z_NW = radius/tan(alpha*pi/360); #Height of nanowire
3 r_clad = radius+clad_t; #Cladding base radius
4 theta = tan(alpha2*pi/360);
5 z_clad = (r_clad)/theta; #Height of cladding
6 xs_tip = r_tip-(r_tip*sin(theta)); #Excess tip height (ht of rounded portion)
7 z_tip = z_clad-r_tip; #Tip length
8 t = (r_tip+r_tip*sin(theta))/2;
9 #1 = Nanowire cone, 2 = Cladding cone, 3 = Cladding tip
10 eqn1 = num2str(radius/z_NW)+"*(x"+num2str(z_NW*(0.5)*1e6)+")";
11 eqn2 = num2str(theta)+"*(x"+num2str(z_tip*(0.5)*1e6)+")"+num2str(r_tip*1e6);
12 eqn3 = "sqrt("+num2str(r_tip*1e6)+"^2-(x"+num2str(t*1e6)+")^2)";
13 #Wire taper
14 addcustom; set("name", "NW_cone");
15 set("x", 0); set("y", 0); set("z", 0);
16 set("create_3D_object_by", "revolution");
17 set("x_span", z_NW); set("y_span", 2*radius); set("z_span", 2*radius);
18 set("equation_1", eqn1); set("first_axis", "y"); set("rotation_1", 90);
19 set("material", NW_mat);
20 if(get("material")=="<Object_defined_dielectric>") { set("index", NW_RI); }
21 #Clad taper
22 addcustom; set("name", "clad_cone");
23 set("x", 0); set("y", 0); set("z", (z_clad-xs_tip-z_NW)/2);
24 set("create_3D_object_by", "revolution");
25 set("x_span", z_clad-xs_tip); set("y_span", 2*r_clad); set("z_span", 2*r_clad);
26 set("equation_1", eqn2); set("first_axis", "y"); set("rotation_1", 90);
27 set("override_mesh_order_from_material_database", 1);
28 set("mesh_order", 3); set("alpha", 0.45); set("material", clad_mat);
29 if(get("material")=="<Object_defined_dielectric>") { set("index", clad_RI); }
30 #Clad tip
31 addcustom; set("name", "clad_tip");
32 set("x", 0); set("y", 0); set("z", z_clad-xs_tip/2-z_NW/2);

```

```

33 set("create_3D_object_by", "revolution");
34 set("x_span", xs_tip); set("y_span", 2*r_clad); set("z_span", 2*r_clad);
35 set("equation_1", eqn3); set("first_axis", "y"); set("rotation_1", 90);
36 set("override_mesh_order_from_material_database", 1);
37 set("mesh_order", 3); set("alpha", 0.45); set("material", clad_mat);
38 if(get("material")==<Object_defined_dielectric>) { set("index", clad_RI); }
39 #Wire base
40 addcircle; set("name", "NW_base");
41 set("x", 0); set("y", 0); set("z", -(z_NW + ht_base)/2);
42 set("radius", radius); set("z_span", ht_base);
43 set("material", NW_mat);
44 if(get("material")==<Object_defined_dielectric>) { set("index", NW_RI); }
45 #Clad base
46 addcircle; set("name", "clad_base");
47 set("x", 0); set("y", 0); set("z", -(z_NW + ht_base)/2);
48 set("radius", r_clad); set("z_span", ht_base);
49 set("override_mesh_order_from_material_database", 1);
50 set("mesh_order", 3); set("alpha", 0.45); set("material", clad_mat);
51 if(get("material")==<Object_defined_dielectric>) { set("index", clad_RI); }
52 #Clad film over substrate
53 address; set("name", "clad_film");
54 set("x", 0); set("y", 0); set("z", -(z_NW/2 + ht_base - clad_t/2));
55 set("x_span", sx); set("y_span", sy); set("z_span", clad_t);
56 set("override_mesh_order_from_material_database", 1);
57 set("mesh_order", 4); set("alpha", 0.45); set("material", clad_mat);
58 if(get("material")==<Object_defined_dielectric>) { set("index", clad_RI); }
59 #Substrate
60 address; set("name", "Substrate");
61 set("x", 0); set("y", 0); set("z", -(z_NW/2 + ht_base + sz/2));
62 set("x_span", sx); set("y_span", sy); set("z_span", sz);
63 set("material", sub_mat);
64 if(get("material")==<Object_defined_dielectric>) { set("index", sub_RI); }
65 #Gates
66 address; set("name", "Gate1");
67 set("x", r_clad + gl/2); set("y", 0); set("z", -(z_NW/2 + ht_base - clad_t - gh/2));
68 set("x_span", gl); set("y_span", gw); set("z_span", gh); set("material", gate_mat);
69 address; set("name", "Gate2");
70 set("x", -(r_clad + gl/2)); set("y", 0); set("z", -(z_NW/2 + ht_base - clad_t - gh/2));
71 set("x_span", gl); set("y_span", gw); set("z_span", gh); set("material", gate_mat);
72 address; set("name", "Gate3");
73 set("x", 0); set("y", r_clad + gl/2); set("z", -(z_NW/2 + ht_base - clad_t - gh/2));
74 set("x_span", gw); set("y_span", gl); set("z_span", gh); set("material", gate_mat);
75 address; set("name", "Gate4");
76 set("x", 0); set("y", -(r_clad + gl/2)); set("z", -(z_NW/2 + ht_base - clad_t - gh/2));
77 set("x_span", gw); set("y_span", gl); set("z_span", gh); set("material", gate_mat);

```

A.3.2 Analysis script

```
1 #Gated_NW_Analysis_Script.txt
2 #Dipole to model quantum dot
3 adddipole; set("name", "QD");
4 set("x", 0); set("y", 0); set("z", zQD); set("theta", 90);
5 set("center_wavelength", QD_center_wavelength);
6 set("wavelength_span", QD_wavelength_span);
7 set("optimize_for_short_pulse", 0);
8 #DFT monitor to extract transmission and far-field profile
9 addpower; set("name", "TFF");
10 set("x", 0); set("y", 0); set("z", zpower);
11 set("x_span", 7e-6); set("y_span", 7e-6);
```

Appendix B

Python code

B.1 Circular two-dimensional Gaussian fit function

```
1 #Fits simulated 2D far-field data from a .csv file to a circular 2D Gaussian
2 #k_x and k_y vectors are also inputted
3 #Output: Data plot with overlaid Gaussian fit contour + R-squared value
4 #Importing libraries
5 import pandas as pd
6 import numpy as np
7 import math as mth
8 from scipy.optimize import curve_fit
9 import pylab as plt
10 #Reading simulated far-field data
11 data = pd.read_csv('data_filename.csv', header = None)
12 data_flat = data.values.ravel() #Flattening to 1D
13 #Importing k-vector for far-field data
14 kxy = pd.read_csv('x_y_vector_500.txt', header=None)
15 klength = len(kxy)
16 #Defining a 2D symmetric circular Gaussian function
17 def twoD_Gaussian(kdata_tuple, amplitude, sigma):
18     (x,y) = kdata_tuple
19     g = amplitude*np.exp( - (x**2 + y**2)/(2*sigma**2))
20     return g.ravel() #Flattening to 1D
21 #Meshing k-vector
22 kx,ky = np.meshgrid(kxy, kxy)
23 #Fitting simulated data to 2D Gaussian using curve_fit
24 initial_guess = [2.8e-12, 0.2] #[amplitude, sigma]
25 popt, pcov = curve_fit(twoD_Gaussian, (kx, ky), data_flat, p0 = initial_guess)
26 data_fitted_flat = twoD_Gaussian((kx,ky), *popt)
```

```

27 data_fitted = data_fitted_flat.reshape(klength, klength) #De-flattening to 2D
28 #Plotting simulated data with best-fit Gaussian overlaid as a contour
29 fig, ax = plt.subplots(1, 1)
30 ax.hold(True)
31 img = ax.imshow(data, cmap=plt.cm.jet, origin='bottom',
32                 extent=(kx.min(), kx.max(), ky.min(), ky.max()))
33 ax.contour(kx, ky, data_fitted, 6, colors='k')
34 plt.xlabel('$k_x$', size = 14)
35 plt.ylabel('$k_y$', size = 14)
36 plt.xlim(-0.4,0.4)
37 plt.ylim(-0.4,0.4)
38 cb = plt.colorbar(img, ax=ax)
39 cb.set_label('$|\overrightarrow{E}|^2 \langle \rangle \langle V^2 m^{-2} \rangle$', size = 14)
40 plt.show()
41 #Calculating R-squared goodness-of-fit
42 residuals = data_flat - data_fitted_flat
43 ss_res = np.sum(np.sum(residuals**2))
44 ss_tot = np.sum((data_flat - np.mean(data_flat))**2)
45 Rsq = 1 - ss_res/ss_tot
46 print(Rsq)

```

Appendix C

Wide 2D p-n junction cleanroom nanofabrication procedure

This procedure was written in collaboration with Dr. Francois Sfigakis and Brandon Buonacorsi. The substrate used in this fabrication process is an undoped GaAs/AlGaAs heterostructure wafer grown using molecular beam epitaxy by the MBE research group. The single heterojunction layer (where the 2DEG forms under an applied potential) lies at the interface of a GaAs and AlGaAs layer at a depth of 310 nm.

C.1 Mesa pattern

1. Sonicate freshly cleaved wafer for 5 min each in Acetone followed by IPA. *As with all new samples make sure to clean the substrate. After cleaving, there is dust that sits on the substrate that will prevent good lithography, and you also want to remove any potential organics on the sample.*
2. 30 s Buffered Oxide Etch (BOE, 1:10 HF:NH₄F by volume) dip. *There is a thin native oxide layer on the sample that needs to be removed, else the resist in the first lithography step will not adhere well, causing issues when etching the mesa.*

3. Spin a PMMA A6/ma-N bilayer. *When spin-coating samples, keep sample covered at all times to prevent dust or other particles from landing on it. Even while baking, use a glass beaker or petridish to cover the sample.*
 - (a) Pre-bake the sample for 1 min at 120°C - *Helps remove any layer of moisture on the sample before you spin the first layer of resist. Be careful not to do too much hotter or longer of a pre-bake as you risk re-forming an oxide layer that will prevent the PMMA from adhering well to the substrate.*
 - (b) While **hot**, spin PMMA A6 at 5000 rpm for 60 s, 1000 rpm/s up-ramp and 1000rpm/s down-ramp. *Be as quick and careful as possible when moving the sample from the hot plate to the spinner before it cools. This will help with adhesion of the PMMA to the GaAs cap layer.*
 - (c) Bake PMMA for 5 mins at 180°C
 - (d) While **warm**, spin ma-N at 5000 rpm for 60 s, 1000 rpm/s up-ramp and 1000rpm/s down-ramp
 - (e) Bake ma-N for 90 s at 120°C
4. Expose the wide-arm Mesa (mask pattern E2): Channel 1, 35 s, soft contact
5. Develop in maD-5335 for 2 mins followed by at least 1 min in H₂O. *Simply place the chip on the bottom of the beaker during development. This eliminates any movement you may introduce which can cause jagged edges and delamination of the two resist layers.*
6. Ash for 10 mins (recipe 11) - *This is to remove the PMMA from the regions we developed the ma-N. Approximately 5 mins is spent removing the PMMA, and the remaining 5 mins are for forming the undercut.*
7. Reflow bake sample at 150°C for 5 mins - *Helps with adhesion of the PMMA to the substrate before we do an etch.*
8. Etch the mesa pattern
 - (a) Dektak the sample to measure resist height

- (b) Dip sample in BOE for 15 s and a 1 min dip in H₂O - *removes any oxide formed from the ashing*
 - (c) Dip sample in a 1:8:120 solution of H₂SO₄:H₂O₂:H₂O (~ 60 - 80 seconds). Use the Dektak to see how much you have etched. While we aim for 350 nm, the exact depth does not matter, but you **must** go past the AlGaAs/GaAs interface (~ 310 nm deep). The typical etch rate is between 3.5 - 5.5 nm/s. *There should be a premixed bottle of 1:120 H₂SO₄:H₂O. Mix 45 mL of this solution and 3 mL of H₂O₂ to get the desired ratio.*
9. Strip the resist by submerging in Acetone and sonicating for 5 - 7 mins. *We can sonicate freely here because there is no metal deposited.*
 10. Dektak the sample to measure actual etched height and confirm the mesa pattern is sharp and clean.

C.2 n-type ohmic contacts

1. Mix a solution of 1:1:9 H₂O₂:HCl:H₂O **the night before** you are going to do the ohmic recess etch.
2. Spin a S1811 layer on main sample. Spin a diluted S1805 layer on an extra sample piece to calibrate the etch rate.
 - (a) Spin resist on each sample at 5000 rpm for 60 s and 1000 rpm/s ramp speed with a ramp down rate of 1000 rpm/s.
 - (b) Bake for 90 s at 120°C
3. Expose the ohmics (pattern E4): Channel 2, 4.5 s, soft contact. Half the ohmics should be covered with tape to prevent their exposure. Only three ohmics to one side should be exposed. *From here on out, whenever you do an exposure, you need to manually decrease the alignment distance until your separation is 0 μm. This helps prevent rotation from the resist beads at the corners of your wafer that act as pivot points when the mask comes in contact for the exposure.*

4. Develop in MF-319 for 45 s and rinse in H₂O. *Mildly agitate, just enough to get the developed Shipley off of your patterned area.*
5. Do a brief 10 sec ash to ensure all Shipley is removed (recipe 5).
6. Reflow bake sample at 150°C for 5 mins.
7. Etch the ohmic pattern
 - (a) Dektak the test etch sample to get resist height. *The reason we used the diluted Shipley is so that the height measured here is more accurate since the resist is so thin.*
 - (b) Dip the test etch sample in BOE for 15 s.
 - (c) Dip test etch sample in H₂O₂:HCl:H₂O etching solution prepared the night before for ~ 70 - 80 s (record the exact time).
 - (d) Dektak the test etch sample again to calibrate the etch rate. Use this rate to calculate how much time it takes to etch to 350 nm. Typical etch rates are ~ 5 nm/s.
 - (e) Dip the main sample in BOE for 10 s.
 - (f) Dip main sample in H₂O₂:HCl:H₂O etching solution for the appropriate amount of time to obtain ~ 350 nm deep recess using rate from test etch sample. *One reason we leave the etch solution overnight is to yield a solution with a stable etch rate. When the solution is first mixed, the etch rate decays rapidly for the first few hours until it equilibrates.*
8. Ash sample for 4.5 min (recipe 11). Simply cancel the recipe after 4.5 min and manually vent. *The goal is to remove as much of the resist overhang made during the wet etch as we can. This will allow us to deposit ohmic material as high up on the wall of our ohmic etch region as possible, making a more reliable and consistent contact to the AlGaAs/GaAs interface where we will induce the 2DEG. Without this etching step, we would not deposit any material on the wall and would have to rely on the diffusion of the metal up towards the interface during the ohmic anneal step.*

9. Dip sample in BOE for 10 s. *We want to make sure there is absolutely **no** oxide between the ohmic and the heterojunction where the 2DEG is formed.*
10. Deposit 10/250/120 nm of Ni/Au+Ge/Ni (0.5/2.0/1.5 A/s deposition rates) in the INTLVAC using the Rotatilt at an angle of 45°. The first layer of Ni helps catalyze the reaction that causes the Ge to diffuse into the GaAs substrate to form a conductive channel to the 2DEG. The Au+Ge is in the ratio 88:12 by weight percentage. The cap layer of Ni is used to help the smoothness of the ohmics after the annealing step. For all layers, use a beam amplitude to focus the beam reducing the required power. *As described above, the Rotatilt ensures that we are depositing ohmic material directly on the interface where we want to form the 2DEG making a good ohmic contact between our ohmic pad. Be careful with the Rotatilt and make sure to select the no rotation profile for the INTLVAC. When connecting the ground and signal cables to the Rotatilt, make sure the tape on the signal line is there to prevent the signal shorting to the ground line during the deposition. The Au+Ge crucible is our own and no other group is allowed to use it.*
11. After deposition, place sample in Remover PG and perform metal liftoff. *Either let it sit overnight at room temperature or place it on a hot plate at 100°C for one hour. Use the spray bottle of acetone to remove any metal pieces clinging to the sample surface.*
12. Anneal the ohmics using the rapid thermal annealer (RTA). Use recipe 'FSUNDOPN' which does a several minute purge with N₂ gas and heats the sample in Ar at 450°C for 3 mins. *It is a good idea to condition the chamber by running the process without a sample once before doing a run with the sample in the chamber. This is not critical but simply an extra precaution against any unwanted contamination a previous user may have introduced.*

C.3 p-type ohmic contacts

1. Mix a solution of 1:1:20 $\text{H}_3\text{PO}_4:\text{H}_2\text{O}_2:\text{H}_2\text{O}$ the night before you are going to do the ohmic recess etch.
2. Spin a S1811 layer on your actual sample. Spin a diluted S1805 layer on an extra sample piece that we will use to calibrate our etch rate.
 - (a) Spin resist on each sample at 5000 rpm for 60 sec and 1000 rpm/sec ramp speed
 - (b) Bake for 90 s at 120°C
3. Expose the ohmics (pattern E4): Channel 2, 4.5 s, soft contact. Rotate the mask 180° to expose the ohmics on the other half of the device.
4. Develop in MF-319 for 35 s and rinse in H_2O - Do mild agitation. Simply enough to get the developed Shipley off of your patterned area.
5. Do a brief ash to ensure all Shipley is removed (recipe 8).
6. Etch the ohmic pattern. *The target etch depth is 20-50 nm above the heterojunction interface.*
 - (a) Dektak the test etch sample to get resist height
 - (b) Dip the test etch sample in BOE for 10 s
 - (c) Dip test etch sample in $\text{H}_3\text{PO}_4:\text{H}_2\text{O}_2:\text{H}_2\text{O}$ etching solution you prepared the night before for ~70-80 s (record the exact time).
 - (d) Dektak the test etch sample again to calibrate the etch rate. Use this rate to calculate how much time it takes to etch to ~290 nm.
 - (e) Dip the real sample in BOE for 10 s
 - (f) Dip real sample in $\text{H}_2\text{O}_2:\text{HCl}:\text{H}_2\text{O}$ etching solution for the appropriate amount of time to obtain ~290 nm depth using rate from test etch sample.
7. Ash sample for 4 min (recipe 11). Simply cancel the recipe after 4 min and manually vent.

8. Dip sample in BOE for 10 s. - We want to make sure there is absolutely NO oxide between the ohmic and the heterojunction where the 2DEG is formed.
9. Deposit 160-200nm of Au+Be onto the sample using a slug weighing 1200-1600 mg in the Angstrom thermal evaporator at an angle of 45°.
10. After deposition, place sample in Remover PG and perform metal liftoff. *Either let it sit overnight at room temperature or place on a hot plate at 100°C for one hour. Use the spray bottle of acetone to remove any metal pieces clinging to the sample surface.*
11. Cap the ohmics with 1 μm of SiO_2 using the PECVD to prevent contamination of the RTA in the subsequent annealing step.
12. Anneal the ohmics using the RTA. Use recipe 'FSUNDOPP' which does a several minute purge with N_2 gas and heats the sample in Ar at 520°C for 3 mins. *It is a good idea to condition the chamber by running the process without a sample once before doing a run with the sample in the chamber. This is not critical but simply an extra precaution against any unwanted contamination a previous user may have introduced.*

C.4 Oxide insulator and via-holes

1. Deposit 300 nm of SiO_2 using the Oxford Cluster. Use the Silane recipe which deposits at 100 nm/min (0.1 nm/cycle). Make sure to clean and condition the chamber prior to deposition even if the previously run process was the same.
2. Spin a S1811 layer on your sample
 - (a) Spin resist at 5000 rpm for 60 s and 1000 rpm/s ramp speed
 - (b) Bake for 90 s at 120°C
3. Expose the vias (pattern E9): Channel 2, 4.5 s, soft contact. *Remember to manually decrease the alignment gap.*

4. Develop in MF-319 for 45 s and rinse in H₂O.
5. Ash for 10 s to remove any resist residue (recipe 5).
6. Dip in BOE for 3 mins. *Check under the scope to make sure you have removed all the oxide in the via areas by looking at the fine alignment marks.*
7. Place the sample in Remover PG and heat to 100°C for 10 mins. Treat the resist removal as a regular metal liftoff. Dry the sample. *We have found that the BOE forms a thin hardened layer of resist during the etching which needs to be removed like a layer of metal when the resist is stripped. If you don't, then the resist layer will fall down onto your sample and can delaminate or flake onto your sample.*

C.5 Top gate and bond pads

1. Spin a PMGI/S1811 bilayer.
 - (a) Pre-bake the sample for 1 min at 120°C.
 - (b) While **hot**, spin PMGI: 5000 rpm for 60 s and 1000 rpm/s ramp with a ramp down rate of 1000 rpm/s.
 - (c) Bake PMGI for 5 mins at 180°C.
 - (d) While **warm**, spin S1811: 5000 rpm for 60 s and 1000 rpm/s ramp with a ramp down rate of 1000 rpm/s.
 - (e) Bake S1811 for 90 s at 120°C.
2. Expose the top gate and bond pad patterns (patterns E8 and F4): Channel 2, 4.5 s, soft contact - *Remember to manual decrease the alignment gap.*
3. Develop in MF-319 for 2.5 mins and rinse in H₂O. *Do not hold the sample during the development step. Simply place the sample in the beaker and step away for the development time. We found that holding the sample during the development can cause the MF-319 to get in between the resist layer and mess up the pattern profile.*

4. Look at the device under the microscope to see if there is a noticeable undercut (1-2 μm). If there is, proceed to the next step. If not, then develop in MF-319 for another 30 seconds and check again. Repeat this until there is a proper undercut.
5. Ash for 10 seconds to remove any resist residue (recipe 5).
6. Dip in 1:4 HCl:H₂O to remove any oxide from ashing. *Do **not** do a BOE dip like you normally would before the deposition. You have sensitive oxide there that will etch away if you do a BOE dip.*
7. Deposit 20/80 nm of Ti/Au (0.5/2.0 A/s deposition rate) in the INTLVAC - *no need for the rotatilt here.*
8. Place in Remover PG for liftoff - *either leave overnight or heat at 100°C for one hour.*